RNF43 mutations facilitate colorectal cancer metastasis via formation of a tumour-intrinsic niche

Jeroen M. Bugter[1], Layla El Bouazzaoui[1, 2, *], Emre Küçükköse[2, *], Yourae Hong[3], Joep Sprangers[1], Ingrid Jordens[1], Nicola Fenderico[1], Diego Montiel Gonzalez[4], Ruben van Boxtel[4], Saskia J.E. Suijkerbuijk[5], Sabine Tejpar[3], Hugo J.G. Snippert[1], Onno Kranenburg[2, ✉], Madelon M. Maurice[1, ✉]

[1]Oncode Institute and Centre for Molecular Medicine, UMC Utrecht, the Netherlands

[2]Department of Surgical Oncology, Lab Translational Oncology, UMC Utrecht, the Netherlands

[3]Department of Oncology, Katholieke Universiteit Leuven, Belgium

[4]Princes Maxima Centre for Pediatric Oncology, Utrecht, the Netherlands

[5]Division of Developmental Biology, Institute of Biodynamics and Biocomplexity, Department of Biology, Faculty of Science, Utrecht University, The Netherlands.

[*]These authors contributed equally to this work

✉ corresponding authors; email: o.kranenburg@umcutrecht.nl & m.m.maurice@umcutrecht.nl

Summary

In colorectal cancer (CRC), *RNF43* mutations are linked to BRAF V600E-initiated serrated adenomas that advance into mucinous adenocarcinomas with poor prognosis upon metastasis. How *RNF43* mutations facilitate a metastasis-prone growth state remains unknown. Here, we addressed this issue by repairing mutant *RNF43* in patient-derived BRAF-mutant CRC organoids using gene editing. Upon *RNF43* correction, CRC organoids exhibit strongly decreased mucus production and, moreover, display loss of niche factor independence and metastatic capacity upon orthotopic transplantation in mice. Mechanistically, we show that mutant RNF43 promotes cancer cell lineage specification towards a non-dividing niche population that secretes essential growth factors, providing a state of self-sufficiency to the cancer epithelium. We show that phenotypic diversification into tumour-intrinsic niche cells (TINCs) and proliferative cancer stem cells depends on tuneable WNT levels enabled by mutations in *RNF43*, but not *APC*. In patient samples, enhanced TINC profiles correlate with *RNF43*-mutant CRC, mucinous histology and metastatic disease, thus representing a general cellular mechanism by which tumours acquire a self-sufficient, pro-metastatic growth state.

Introduction

Self-renewal of human colon adult stem cells is controlled by specialized epithelial and mesenchymal niche cells that secrete essential factors to promote growth and prevent differentiation[1]. Identification of the essential stem-cell niche factors such as WNT, EGF and BMP-antagonists has led to the establishment of *in vitro* culture conditions for intestinal organoids[2]. Different from healthy adult colon stem cells, patient-derived colorectal cancer (CRC) cells commonly display loss of niche factor-dependency during *in vitro* outgrowth into organoids, which correlates with their metastatic capacity *in vivo*[3,4]. In the classical view, the adenoma-carcinoma transition is driven by an accumulation of mutations (e.g. *APC/KRAS/SMAD*) that endow tumour cells with stem cell-like properties while omitting the need for a specialized niche[3–5].

CRC is however a heterogeneous disease and can develop via two mutually exclusive genetic pathways with distinct molecular and clinical manifestations[6–9]. 15-30% of sporadic CRCs develop via a distinct route, commonly referred to as the serrated neoplasia pathway that is typically initiated by an oncogenic BRAF mutation and is mutually exclusive with WNT activating APC mutation. In contrast to *APC*-induced adenomas, serrated lesions do not present with an expansion of the classical stem-cell program and retain properties related to differentiated colon epithelium[9]. Upon acquiring a mutation in the negative WNT pathway regulator RNF43, serrated lesions can advance into mucinous adenocarcinomas with poor prognosis upon metastasis[9–12] Despite their frequent occurrence, the mechanism by which *RNF43* mutations contribute to tumour progression and metastatic spread has thus far remained unclear.

Importantly, *RNF43/BRAF*-mutant CRC remains sensitive to inhibition of upstream WNT and EGF signalling[4,13,14]. Notwithstanding their WNT dependence, *RNF43/BRAF*-mutant tumours are characterized by relatively low levels of WNT target gene expression and high

mucus production[15]. How these epithelial cancer subsets acquire the capacity to generate their own growth factors to drive a self-sufficient growth state remains unknown.

Here, we investigated the functional driver role of *RNF43* mutations in late stage, metastasis-prone BRAF V600E-mutant mucinous adenocarcinoma. We employed CRISPR-mediated gene editing to repair RNF43 mutations in patient-derived CRC organoids, and examined consequences for cancer epithelial organization, growth factor dependencies and *in vivo* tumour growth and metastatic capacity. Our findings uncover a driver mechanism that involves the formation of specialized niche-factor producing cells, which permits an autonomous, pro-metastatic growth state that relies on self-organized interactions between dividing and non-dividing cancer cell populations.

Results

RNF43 mutation repair in patient-derived organoids eliminates metastatic capacity and niche-independent outgrowth

To investigate whether common differences in transcriptional profiles between *RNF43*-mutant and *APC*-mutant CRC are maintained in organoid culture conditions, we compared RNAseq data of a panel of representative human patient-derived CRC organoids (Figure 1A). In agreement with previous reports[6,9,15], *RNF43*-mutant CRC organoids displayed relatively low levels of WNT target gene expression and an increased expression of mucin-related genes (Figure 1A). To address the functional driver role of mutated *RNF43*, we selected the *RNF43/BRAF*-mutant human CRC organoid line HUB040, derived from a primary human mucinous colorectal adenocarcinoma that presented with prominent metastasis in the patient[16]. Different from healthy colon organoids[4,13], HUB040 can be propagated without supplementation of WNT, RSPO and EGF, indicating that this tumour acquired a state of growth factor self-sufficiency (Figure 1B). As expected, based on its *RNF43*-mutant status, HUB040 was sensitive to treatment with Porcupine inhibitors, confirming its dependency on

self-produced WNTs (Figure 1C) [4,13]. We employed gene editing to correct the mutated *RNF43* locus to wildtype and obtained two *RNF43*-corrected clones (RC1, RC2) and one non-corrected control clone (NC1) (Figures 2A and 2B). Whole genome sequencing of all clones confirmed preservation of pre-existing HUB040 driver mutations, other than *RNF43* (Figure S1A). Karyotypes of HUB040, NC1 and RC2 were similar, while RC1 was somewhat divergent, mainly due to whole genome duplication (Figures S1B-G). To investigate metastatic capacity, we performed orthotopic transplantation of organoids into the caecal wall of immune-deficient mice[17]. After 120 days, HUB040 and NC1 had formed primary tumours that spontaneously metastasized to the lungs and the liver (Figures 2C, 2D and S2A). Strikingly, for transplanted *RNF43*-corrected organoids no metastatic lesions were detected (Figures 2C and 2D), even though their primary tumour load equalled that of *RNF43*-mutant counterparts (Figure S2A). Thus, by restoring a single mutation we eliminated the metastatic capacity of this aggressive cancer model. These data suggest a key role for mutated *RNF43* in promoting metastasis.

Next, we assessed organoid niche-independency by performing single cell reconstitution assays in growth factor-depleted conditions. Like HUB040, *RNF43*-mutant NC1 organoids retained their capacity to expand in medium lacking extrinsic growth factors (Figures 2E, S2B and S2C). By contrast, *RNF43*-repaired lines RC1 and RC2 acquired a strong dependence on supplementation with WNT, RSPO and EGF (Figures 2E, S2B and S2C). These results were unexpected, as introduction of *RNF43* mutations in healthy human colon-derived or mouse intestinal organoids are known to enhance WNT sensitivity[10], but are not known to alter EGF dependency. Our data thus imply a role for *RNF43* mutations in promoting cancer cell survival and growth in the absence of growth factor supplementation.

Mutant *RNF43* drives mucinous differentiation and niche factor production

We next aimed to investigate how *RNF43* mutations affect tumour phenotype. Transcriptome comparison of HUB40, NC1 and both RC organoid lines yielded a mutant *RNF43*-driven gene expression signature that comprised numerous genes encoding growth factors and mucins (Figures 3A, 3B, S2D and S2E). In line with these findings, gene sets representing Goblet and Deep Crypt Secretory (DCS) cells of healthy colon were significantly depleted from RC1 and RC2 in comparison to control lines (Figure 3C)[18,19]. Furthermore, *RNF43*-mutant tumours displayed extensive mucus secretion *in vitro* and *in vivo*, while this property was strongly diminished upon *RNF43* correction (Figures 3D-F), strengthening the observation that *RNF43* mutations facilitate secretory cell differentiation.

Notably, the *RNF43*-mutant signature comprised several reported niche factors including *IGF2*, *VEGFA*, *DLL1/4* and *WNT8B* (Figures 3A, 3B and S2E). Blocking upstream IGF and WNT signalling diminished reconstitution capacity of HUB40 CRC organoids, which was rescued by supplementation with exogenous EGF or WNT ligands, respectively (Figures 3G and 3H), reminiscent of the growth state of *RNF43*-corrected organoids (Figures 2E and S2B). Based on these data, we hypothesized that *RNF43* mutations accommodate the production of self-produced niche-factors that are essential for tumour survival and growth. To test this, we generated hybrid co-cultures of *RNF43*-mutant and *RNF43*-corrected organoids and monitored them over time in growth factor-depleted medium using live imaging (Figure 3I and Supplementary Videos 1-2)[20]. While cultures of unmixed *RNF43*-corrected organoids displayed a high ratio of cell death over mitotic events, this ratio was reversed when *RNF43*-corrected cells shared a lumen with *RNF43*-mutant cells (Figure 3J). These results confirm that HUB040 CRC survival relies on paracrine signalling events that are facilitated by mutant RNF43.

Mutant *RNF43* promotes tumour-intrinsic niche cell formation.

In a previous study, we showed that inactivation of *Rnf43* and its paralogue *Znrf3* in the mouse small intestine induces hyperplasia of stem cells as well as secretory Paneth cells, that function as an intra-epithelial stem cell niche[21,22]. To investigate how *RNF43* mutations may promote the formation of specialized niche factor-producing cells within human CRC, we first performed single cell RNA sequencing analysis of the HUB040 organoid line. Single cell profiles spanned seven clusters with distinct expression patterns discovered by unsupervised clustering (Figures 4A and S3A). Noticeably, one population of cells (cluster 1), representing about one-sixth of tumour cells, entirely lacked expression of proliferation and stem cell-related genes[23] (Figures 4B, 4C and S3B). Instead, this subset displayed prominent hallmarks of differentiated secretory niche cells, as exemplified by the expression of gene sets related to Goblet cells (Figure 4D), Deep Crypt Secretory (DCS) cells (Figure 4E)[18,19], hypoxia and glycolysis (Figures S3C-E)[24,25], as well as mTOR activation and the unfolded protein response (Figure S3E)[26–28]. We thus identified cluster 1 as a non-proliferating, niche factor-producing secretory cancer cell subset that we call tumour-intrinsic niche cells (TINCs).

Subjection of healthy colon organoids to growth factor depletion caused emergence of a TINC and DCS signature-enriched cell population, supporting the observation that TINCs share identity with differentiated, healthy DCS cells (Figure S4)[18]. Notably, the TINC gene signature was significantly downregulated in both RNF43-corrected clones (Figure S3F). scRNAseq analysis of all clones in complete medium revealed that 16% of both HUB040 and NC1 cells displayed high expression of the full TINC signature which was reduced to 1-7% of cells within RNF43-corrected clones (Figure 4F). In agreement, expression of prominent TINC markers was diminished in RNF43-corrected clones (Figure 4G). Based on these findings, we conclude that TINC formation is promoted by mutant RNF43.

***RNF43*-mutant organoids self-organize into proliferating stem cells and non-proliferating supporting niche cells**

To characterise mutant *RNF43*-dependent TINC cells, we focussed on *NDRG1*, that we identified as a prominent marker gene for TINCs in HUB40 organoids, and for DCS cells in healthy colon organoids (Figures S3G and S4I). Introduction of an IRES-linked mNeon green fluorophore within the *NDRG1* gene revealed that TINCs are heterogeneously distributed within HUB040 (Figures 4H, 4I and S5A). Non-dividing NDRG1^{high} TINC reporter cells were interspersed with proliferative NDRG1^{low} cells as shown by KI67 labelling (Figure 4I) and EdU incorporation (Figure 4J). Despite their differentiated and non-proliferative appearance, TINCs retained regenerative capacity, as isolated NDRG1^{high}, NDRG1^{medium} and NDRG1^{low} single cells gave rise to fully grown organoids in which the heterogeneous distribution of TINCs was restored (Figures 4K and S5B). Our data thus reveal that *RNF43/BRAF*-mutant HUB040 CRC organoids display phenotypic heterogeneity and are capable of self-organising into a mixture of non-proliferative TINCs and stem-like cell populations.

An in-depth transcriptome characterization of sorted NDRG1^{high} cells compared to sorted NDRG1^{medium} and NDRG1^{low} cells (Figures S5C-E) generated an 'extended TINC signature' of about 1.000 genes that robustly confirmed previously identified TINC hallmarks (Figures S5F, S5G and S3E), including mutant *RNF43*-dependent niche factors such as *IGF2, Dll1, IGFBP2* and *VEGFA* (Figures 4L and 3M). Intriguingly, TINCs displayed a relatively decreased expression of WNT target genes, including *RNF43* itself (Figure 4M). These results support a model in which *RNF43* mutations allow for tuneable WNT signalling and intra-tumoural lineage diversification, even though all cells are *RNF43*-mutant. Lastly, marker genes related to regeneration (*ANXA1*) and metastatic relapse (*EMP1*) were enriched in TINCs (Figure 4M)[29,30]. We conclude that *RNF43* mutations facilitate tumour cell differentiation into niche

factor-producing cells, which explains the acquired niche-independent growth state of these tumours.

TINCs are enriched in *RNF43*-mutant human CRC and metastatic lesions

We next explored the broader relevance of TINCs for human CRC. TINC marker gene expression was significantly enriched in *RNF43*-mutant as well as mucinous CRC subtypes of the cancer genomics atlas (TCGA) (Figures 5A and 5B). Moreover, TINC gene expression was significantly enhanced in lung and liver metastases compared to primary colorectal tumours (Figures 5C and S6A). At the single cell level, CRC tumours were recently classified into two intrinsic epithelial subtypes[6]. Among these, TINC signature expression was highest in the iCMS3 group, in which *RNF43* mutations are predominantly found (Figure 5D)[6]. Furthermore, within iCMS3 tumours, TINC signature expression was higher in *RNF43*-mutant compared to *RNF43* wildtype cases (Figure 5D). We corroborated these findings by re-analysis of 18.320 single cell transcriptomes derived from CRC tumours of 28 patients, of which four were *RNF43* mutant[6] (Figure S6D). Supervised clustering with batch correction resolved eight shared CRC cell clusters. In comparison with *RNF43* wildtype CRC, *RNF43*-mutant CRC accumulated a larger fraction of cells within two clusters (cluster 3 and 5) (Figures 5E, 5F and S6E) that were enriched for *RNF43*-regulated genes (Figure S6G). Additionally, cluster 5 was enriched for goblet cell markers, while TINC markers mapped to cluster 3, exemplified by high *NDRG1* expression (Figures 5G and S6G). Thus, *RNF43*-mutant CRC subsets are not only enriched for TINC marker expression but also display an overall increased fraction of TINCs (Figure S6F).

Tuneable WNT signalling balances the formation of stem cells and supporting tumour niche cells.

The fraction of TINCs was lowest in iCMS2 subgroups that is often driven by *APC* mutations and high WNT signalling (Figure 5D)[6]. In line, TINC marker gene expression inversely correlated with high WNT signalling and *APC* mutations when analysed in TCGA (Figures S6B and S6C). To investigate how *APC* mutations affect WNT signalling and TINC formation in context of a non-iCMS2 tumour, we introduced a conventional truncating mutation in the *APC* mutation cluster region of the HUB040 organoid. Surprisingly, and in contrast to healthy colon organoids[31], biallelic targeting of *APC* was rather inefficient in HUB040 (Figure S7A), in line with the observed mutual exclusivity of *APC* mutations in *BRAF/RNF43*-mutant human cancers[32]. Compared to HUB040$^{APC+/-}$ clones that we obtained, HUB040$^{APC-/-}$ organoid clones displayed prominent WNT/β-catenin target gene expression, enhanced nuclear β-catenin levels and acquired resistance to treatment with WNT secretion inhibitors (Figures 6A, 6B and S7B-D). Furthermore, introduction of truncated APC induced enrichment of gene signatures representing transit amplifying (TA) cells and stem-like cells, while secretory cell profiles and the TINC signature were significantly reduced (Figures 6C and 6D)[33]. Single cell analysis revealed that introduction of an *APC* mutation shifted HUB040 cell identity and composition, as shown by an increased fraction of WNT-high cells and a reduced fraction of cells expressing the TINC signature (Figures 6E, 6F and S7E-G). These alterations were not compatible with efficient growth, as HUB040$^{APC-/-}$ organoids were outcompeted by HUB040^{APCwt} organoids during co-culture (Figure 6G). We conclude that *APC* mutations, in context of a *BRAF/RNF43*-mutant tumour background, interfere with intra-epithelial niche formation that is otherwise facilitated by mutant *RNF43*.

We hypothesized that adjustable levels of WNT signalling are vital for *BRAF/RNF43*-mutant tumour self-organising capacity. Indeed, constitutive pharmacological activation of WNT signalling (CHIR99021) was not tolerated by HUB040 organoids (Figure 6H). Furthermore, HUB040 organoids treated with WNT inhibitors for 24 and 48 hours (Figures

S7H-J) revealed an incremental downregulation of proliferative, stem and TA signatures and an increase in differentiation signatures, including TINC (Figures 6C and 6D). In line with these findings, the number and brightness of TINC reporter cells in HUB040 increased upon WNT inhibitor treatment (Figures 6I and S7K). Thus, although *BRAF/RNF43*-mutant mucinous cancers are wired towards lower levels of WNT signalling that are optimal to facilitate secretory differentiation, a threshold of WNT signalling in a subset of cancer cells is still required to prevent terminal differentiation and maintain self-renewal of proliferative cells (Figure 6J).

Discussion

Self-organisation principles promote tumour progression in CRC[34–41], but thus far the underlying genetic driver events remained poorly understood. In this study, we show that *RNF43* mutations facilitate the generation of TINCs, tumour-intrinsic NDRG1^{high}/VEGFA^{high} niche cells that secrete essential growth factors to drive proliferation and survival of adjacent stem-like cancer cells. Despite their differentiated, non-proliferative phenotype, TINCs retain phenotypic plasticity and can give rise to full-blown tumour structures.

Different from classical *APC* mutations that promote uniform high WNT signalling and endow tumour cells with stem-like properties, we find that mutant *RNF43* permits for tuneable WNT activity, which enables tumour cells to pick diverging phenotypic states. Accordingly, *RNF43* mutations drive a growth state that relies on interactions between dividing and non-dividing cancer cell populations (Figure 6K). This role of mutant *RNF43* is reminiscent of the concomitant hyperplasia of stem cells and Paneth niche cells induced by co-deletion of *Rnf43/Znrf3* from the mouse small intestine[21]. In human colon cancer development, however, *RNF43* mutations arise after tumour-initiating *BRAF* mutations[9,10,32]. Consistently, our results indicate that *RNF43* mutations are crucial for metastatic spread, but not for tumour initiation. As both niche independency and phenotypic plasticity correlate with metastatic capacity in

CRC[4,38,40,41], it is tempting to speculate that mutant *RNF43*-mediated TINC formation is a prerequisite for metastasis to distant organs. In line with this assumption, we find that TINC profiles are enhanced in metastatic samples of mucinous human CRC.

Strikingly, introduction of *APC* mutations in a *BRAF/RNF43*-mutant context suppresses TINC formation and is not beneficial for growth of this tumour subtype, indicating that cancer driver activity of WNT mutations relies on a specific mutational context. Furthermore, the dependence of *BRAF*/*RNF43*-mutant tumours on adjustable WNT signalling for establishing a tumour-intrinsic niche offers an opportunity for pharmacological interference. While constitutive enhancement of WNT signalling in these tumours precludes niche formation and growth factor self-sufficiency, inhibition of WNT pushes terminal differentiation and stem cell depletion. Notwithstanding the clear regulatory role of WNT, other pathways may play a role in TINC formation. *RNF43* truncating mutations were recently linked to activation of the PI3K-Akt-mTOR pathway[42], which also mediates activation of cellular programs linked to glycolysis and hypoxia[43], as well as Goblet and Paneth cell differentiation in the mouse intestine and human intestinal organoids[27,28,44,45].

Additionally, we demonstrate that *RNF43* mutations are causative to a mucinous CRC phenotype. How excessive mucus production links to cancer development and metastasis formation remains incompletely understood[46], although roles in immune evasion, growth factor trapping and chemoprotection were proposed[47]. We expect that formation of an intra-tumoral pro-metastatic mucinous niche is relevant for other *RNF43*-mutant human cancers with mucinous histology, including intraductal mucinous carcinoma of the pancreas and mucinous ovarian cancer[48–50].

In summary, our study demonstrates that genetic correction of putative driver genes in patient-derived organoids is a powerful approach to examine the mechanistic role of these mutations in an advanced human cancer context. Our findings predict that *RNF43*-mediated

tumor-intrinsic niche formation is a broad concept in cancer biology, and that a comprehensive understanding of the pathways and mechanisms underlying tumour niche self-organization are likely to provide insights that may be harnessed to help limit disease progression and metastatic recurrence.

Acknowledgements

The authors thank members of the Maurice laboratory for helpful discussions and suggestions. We thank Bas Ponsioen for help with time-lapse image analysis. This work is part of the Oncode Institute, which is partly financed by the Dutch Cancer Society. This work was supported by the Netherlands Organization for Scientific Research NWO VICI Grant 91815604 (to M.M.M) and ZonMW TOP Grant 91218050 (to M.M.M., O.K. and H.J.G.S.), the IMAGINE! Gravitation grant 024.005.009 (to M.M.M. and H.J.G.S.), and Dutch Cancer Society Young Investigator Grant 11491/2018-1 (to S.J.E.S.).

Author Contributions

J.M.B., L.E.B., E.K., H.J.G.S., O.K. and M.M.M. conceptualized the project. J.M.B., O.K. and M.M.M. designed and interpreted experimental results. J.M.B. generated CRISPR lines, performed all *in vitro* organoids experiments and analysed single-cell and bulk RNAseq data, E.K. performed *in vivo* transplantation experiments and immunohistochemistry, L.E.B. prepared the PDO panel for RNAseq (Figure 1C), Y.H. and S.T., provided and analysed single-cell RNAseq patient data, J.S. designed and cloned the TINC-reporter construct and advised on single cell RNAseq analysis. I.J. performed FACS sorting and helped with image processing and analysis. N.F. designed the CRISPR strategy for *RNF43* correction and performed C59 experiments. D.M.G. and R.V.B. analysed and interpreted genomics data. S.J.E.S. performed time-lapse imaging and advised on hybrid co-culture experiments. J.M.B. and M.M.M. wrote the manuscript, which was reviewed by all authors.

Declaration of interests

Madelon Maurice is cofounder and shareholder of Laigo Bio B.V. The other authors declare no competing interests.

Figures

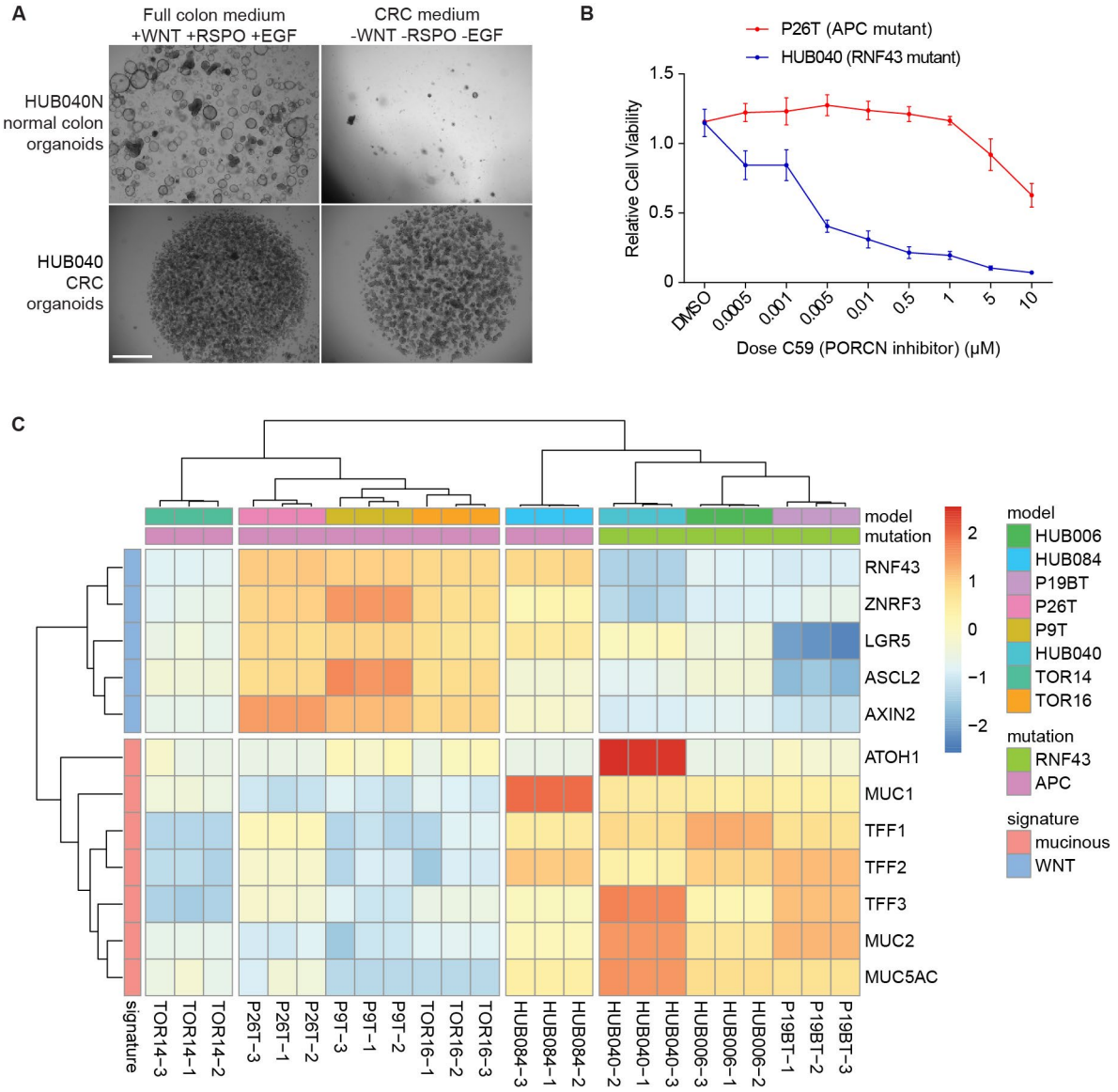

Figure 1 | Patient-derived *RNF43*-mutant CRC organoids are growth factor self-sufficient. A. Heatmap of gene expression data for WNT markers or mucinous markers over a panel of CRC organoids (n = 8). Presence of *RNF43* or *APC* mutation is indicated on top. Unsupervised clustering into four groups shows that *RNF43*-mutant organoids cluster together in a low-WNT, high-mucinous group. Coloured bar represents row z-scores of normalised counts. **B.** Representative brightfield images showing healthy colon organoids and HUB040 CRC organoids cultured in CRC culture medium or complete colon organoid medium

(including WNT, EGF and RSPO) for one passage and 14 days in total. Scale bar = 1000 µm. **C.** Line graphs showing normalized viability of HUB040 and P26T organoids treated with indicated concentration of PORCN inhibitor C59 for 7 days. Data were normalized to PBS-treated organoids. n = 2, mean + sd

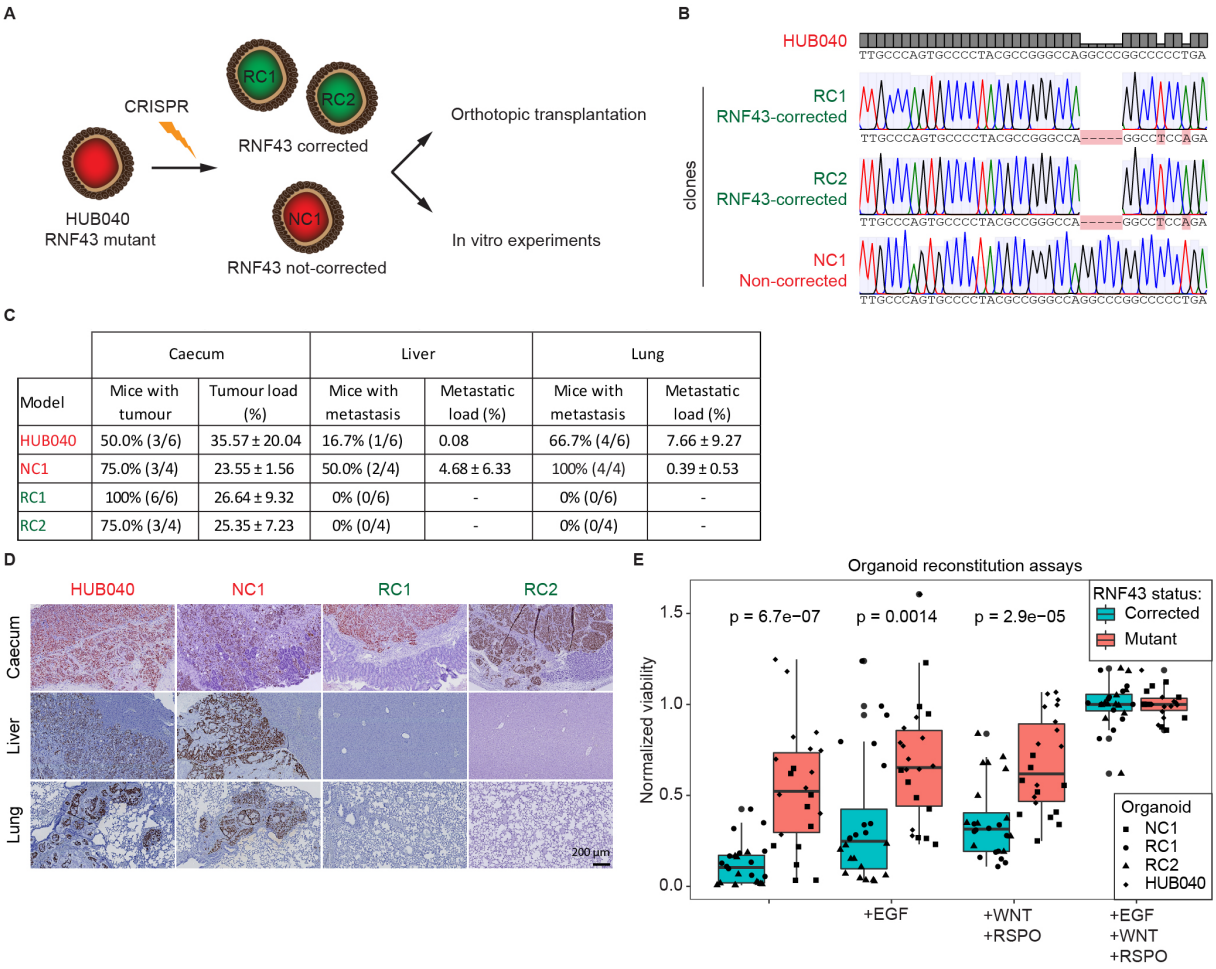

	Caecum		Liver		Lung	
Model	Mice with tumour	Tumour load (%)	Mice with metastasis	Metastatic load (%)	Mice with metastasis	Metastatic load (%)
HUB040	50.0% (3/6)	35.57 ± 20.04	16.7% (1/6)	0.08	66.7% (4/6)	7.66 ± 9.27
NC1	75.0% (3/4)	23.55 ± 1.56	50.0% (2/4)	4.68 ± 6.33	100% (4/4)	0.39 ± 0.53
RC1	100% (6/6)	26.64 ± 9.32	0% (0/6)	-	0% (0/6)	-
RC2	75.0% (3/4)	25.35 ± 7.23	0% (0/4)	-	0% (0/4)	-

Figure 2 | Repair of *RNF43* mutations in patient-derived organoids blocks metastasis and niche-independent outgrowth. A. Schematic of experimental setup of this study. **B.** Sanger sequencing traces of *RNF43*-corrected clones (RC1, RC2) and non-corrected control clone (NC1) compared to the locus of the HUB040 CRC organoid. **C.** Table showing tumour forming efficiency and tumour/metastatic load in caecum, liver and lung, 120 days after transplantation. Tumour and metastatic load were determined as human nucleoli area over total tissue area. **D.** Representative human nucleoli stainings of caecum, lung and liver of mice, 120 days after

transplantation of indicated HUB040 clones. Scale bar = 200 µm **E.** Normalized viability of *RNF43* mutant and *RNF43*-corrected HUB040 clones treated as in Figure S2B. Results of six experiments are presented, including one to three replicates per condition per experiment (n =12 per condition in total). Data are normalised against mean value in complete medium per experiment. Kruskal-Wallis test is used to compare *RNF43* mutant and corrected within each condition.

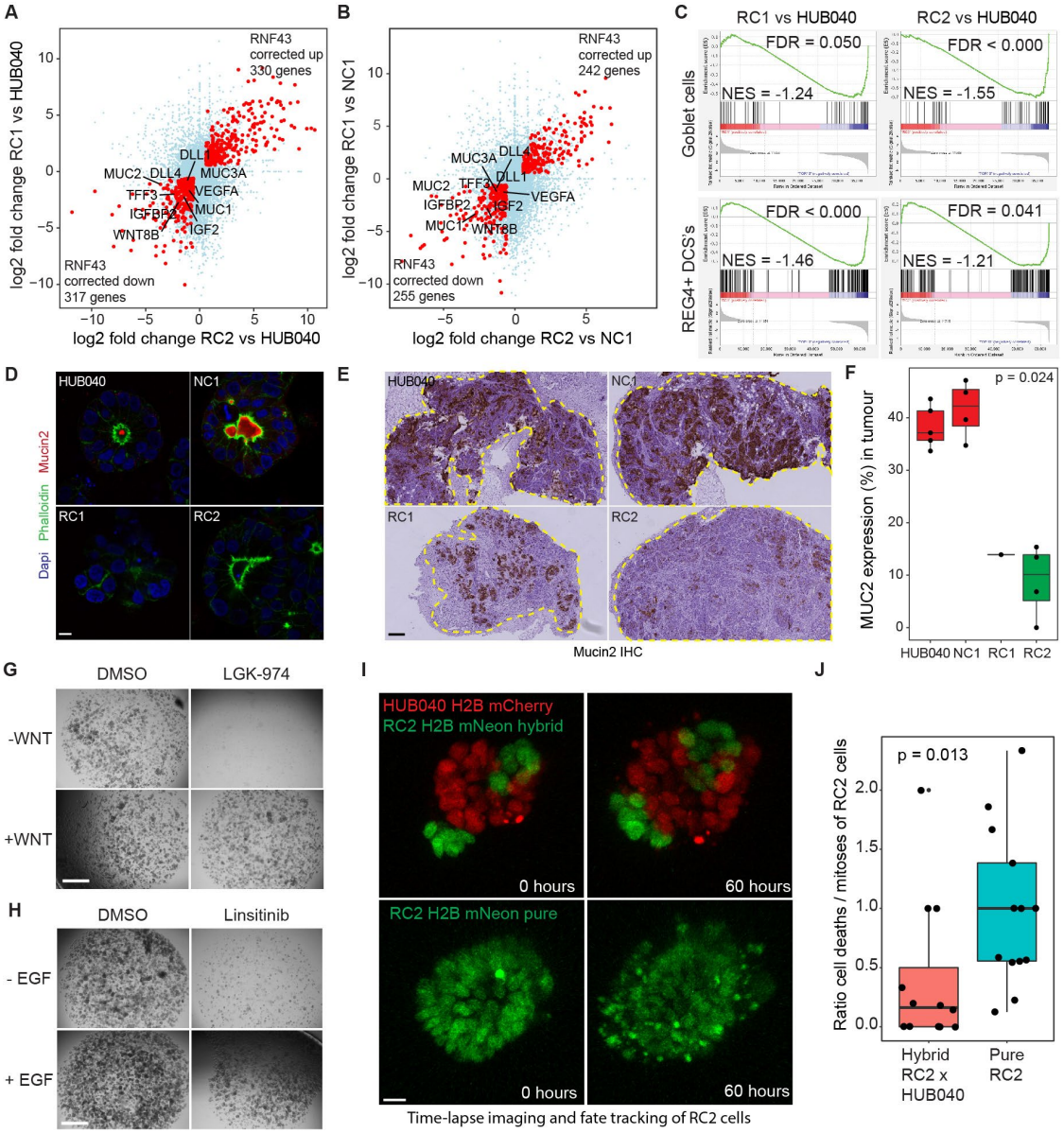

Figure 3 | Mutant *RNF43* drives mucinous differentiation and niche factor production. A, B. Scatter plots showing log2 fold change of gene expression between *RNF43*-corrected clones, RC1 (Y-axis) and RC2 (X-axis), and HUB040 (**A**) or non-corrected clone 1 (NC1) (**B**). Genes with significant differential expression (FC > 1.5 and $p < 0.05$) in both comparisons are indicated as larger red dots. Downregulated genes of interest are annotated. Total number of genes that are up- or downregulated in both comparisons is plotted in the corners. **C.** GSEA plots showing enrichment of a colonic goblet cell signature[19] and REG4+ deep crypt secretory cell (DCS) signature[18] in HUB040 compared to RC1 or RC2. **D.** Representative confocal microscopy images of organoids stained for mucin2 (MUC2, in red), actin (phalloidin, green) and nuclei (dapi, blue). Scale bar = 10 µm. **E.** Representative IHC images for mucin2 (MUC2) on primary subcutaneous tumours. Scale bar = 250 µm. **F.** Box plots showing the percentage of MUC2+ tumour area in primary subcutaneous tumours. Significance was evaluated using a Krusak-Wallis test. **G, H.** Representative low-magnification brightfield images of HUB040 organoids treated with 100 nM PORCN inhibitor LGK-974 (**G**), 1 µM IR/IGFR inhibitor Linsitinib (**H**) or DMSO in CRC culture medium with or without WNT surrogate (**G**) or EGF (**H**) supplementation for 14 days, passaged after 7 days. Scale bar = 1000 µm. **I.** Representative 3D projected images of time-lapse series of hybrid HUB040-RC2 or pure RC2 organoids in CRC medium at the start and end of the time-lapse; nuclei are visualized by expression of H2B-mNeon or H2B-mCherry. Scale bar represent 20 µm. **J.** Result of analysis of RC2-cell fate over time in the two conditions. Cell death and mitotic events were counted for all RC2-H2B-mNeon cells in 13-14 movies per condition. The ratio of number of cell death over mitotic events is shown.

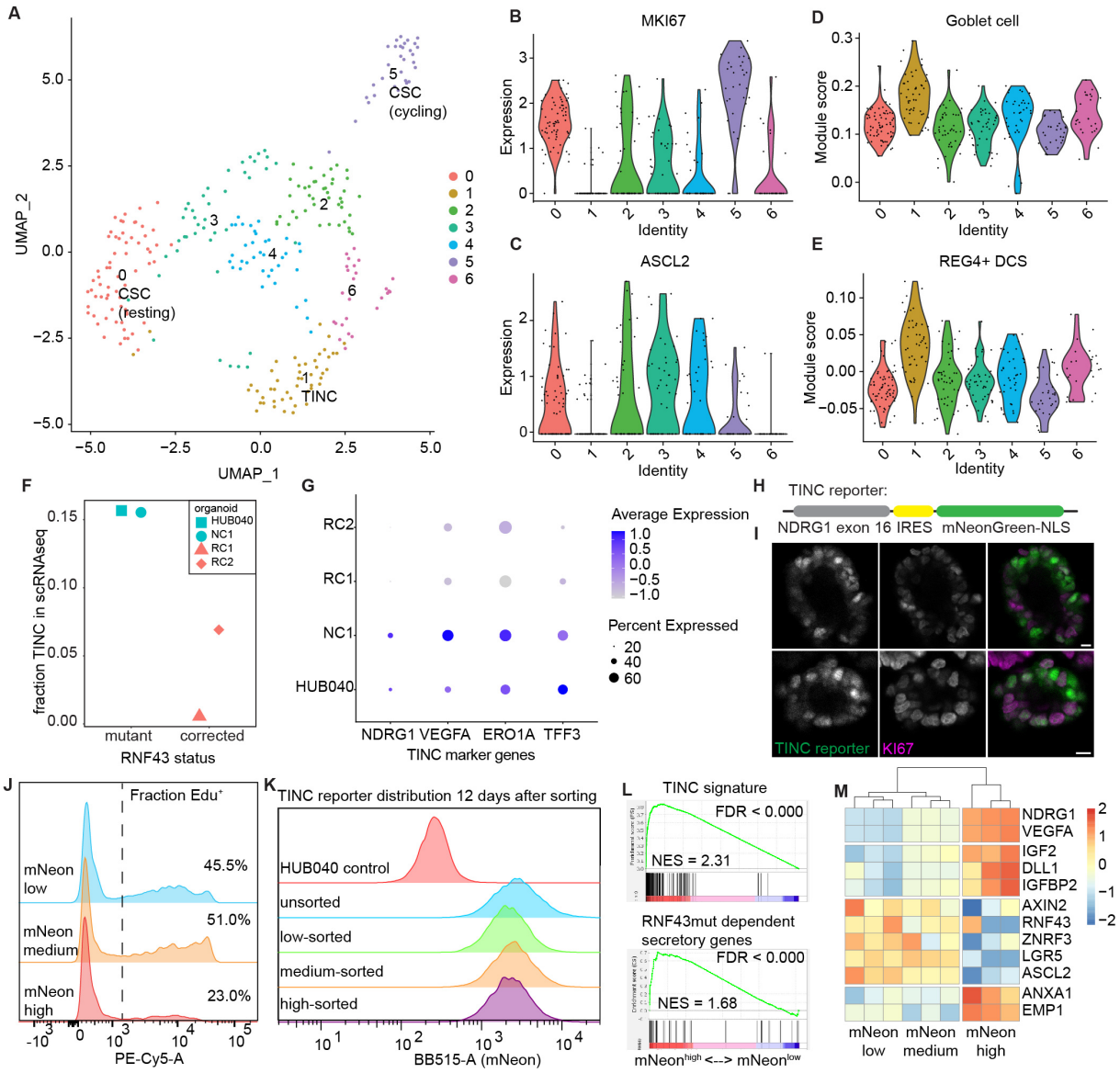

Figure 4 | Mutant *RNF43* promotes tumour-intrinsic niche cell formation. A. Reduced dimensionality (UMAP) visualisation of single cell RNA sequencing data of HUB040 organoids cultured in CRC medium. Results of unsupervised clustering are colour-coded per cluster. **B, c.** Violin plots showing scaled single cell expression levels of proliferation marker MKI67 (**B**) and cancer stem-cell marker ASCL2 (**C**) grouped by cluster. **D, E.** Violin plots showing single cell module scores for expression of genes from a colonic goblet cell signature[19] (**D**) and REG4+ deep crypt secretory cell (DCS) signature[18] (**E**) grouped by cluster. **F.** Plot showing the fraction of cells that were scored as TINC in the analysis of single cell RNA sequencing data of the four indicated organoid lines. **G.** Dot-plot showing the average

expression and fraction of cells expressing indicated TINC marker genes. **H.** Schematic of the endogenous TINC reporter construct. **I.** Representative confocal microscopy pictures of TINC reporter-positive cells (mNeon) in HUB040 organoids, combined with KI67 immunostaining. Scale bar = 10 µm. **J.** FACS plot of HUB040 TINC reporter organoids gated for low, medium or high mNeon signal showing the result of EdU labelling after 16h incubation with EdU. **K.** Histograms showing distribution of mNeon fluorescence by FACS of TINC reporter organoids that were sorted according to Figure S5A into mNeon-high, -medium and -low cells and allowed to reconstitute into heterogeneous organoids for 12 days. **L.** GSEA plots showing enrichment of the TINC signature that was derived from single cell RNAseq and the 'RNF43-mutation dependent secretory gene signature' as defined in Figure S2E for TINC reporter high versus low cells. **M.** Heatmap showing Z-scores for the expression of selected genes (TINC markers, growth factors, WNT target genes and regenerative genes) in the TINC reporter low, medium and high cells.

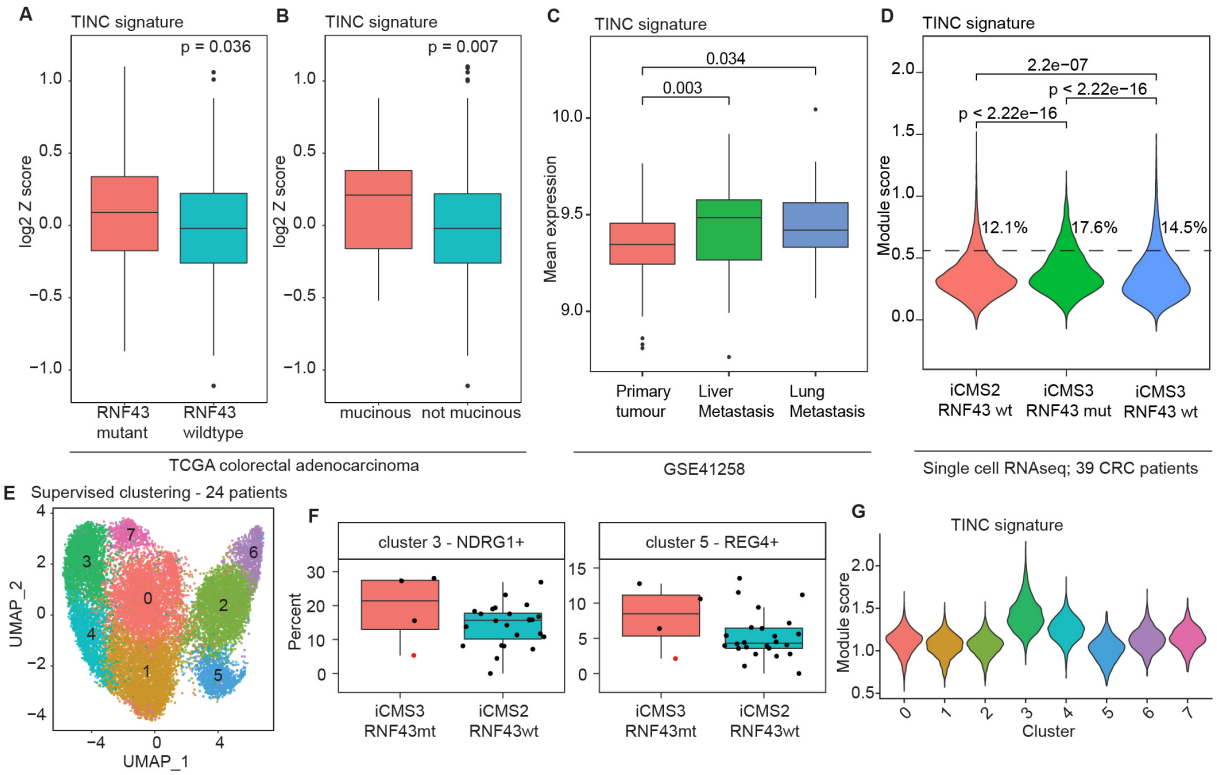

Figure 5 | TINCs are enriched in *RNF43* mutant CRC patients and metastatic lesions. A, B. Box plots showing log2 Z-scores for the TINC signature (top 25 differentially expressed marker genes of HUB040 cluster 1 as determined in single cell RNAseq analysis) over the colon adenocarcinoma TCGA bulk RNA sequencing dataset grouped by *RNF43*-mutation status (n = 46 mut, 337 wt) (**A**) or pathology classification as mucinous (n = 37) or non-mucinous (n = 346) (**b**). **C.** Box plots showing expression of TINC signature (RMA normalization data) in microarray data of 186 primary tumours, 48 liver metastases and 20 lung metastases.[51] **D.** Violin plot showing single cell module scores for expression of genes from the TINC signature of single cells from 39 patients of Joanito et al[6] (iCMS2, 25 patients; iCMS3_RNF43wt, 10 patients; iCMS3_RNF43mut, 4 patients). Percentage of cells scoring above threshold of 0.55 is indicated. **E.** Reduced dimensionality (UMAP) visualisation of supervised clustering using 154 TINC signature genes of 18.320 single cells from 28 patients by Joanito et al[6]. **F.** Box plots showing the fraction of cells in cluster 3 or 5, divided by *RNF43* mutation status per patient.

The red dot marks a patient that has a *RNF43* and *APC* mutation. **G.** Violin plot showing single cell module scores for expression of genes from the TINC signature grouped by cluster.

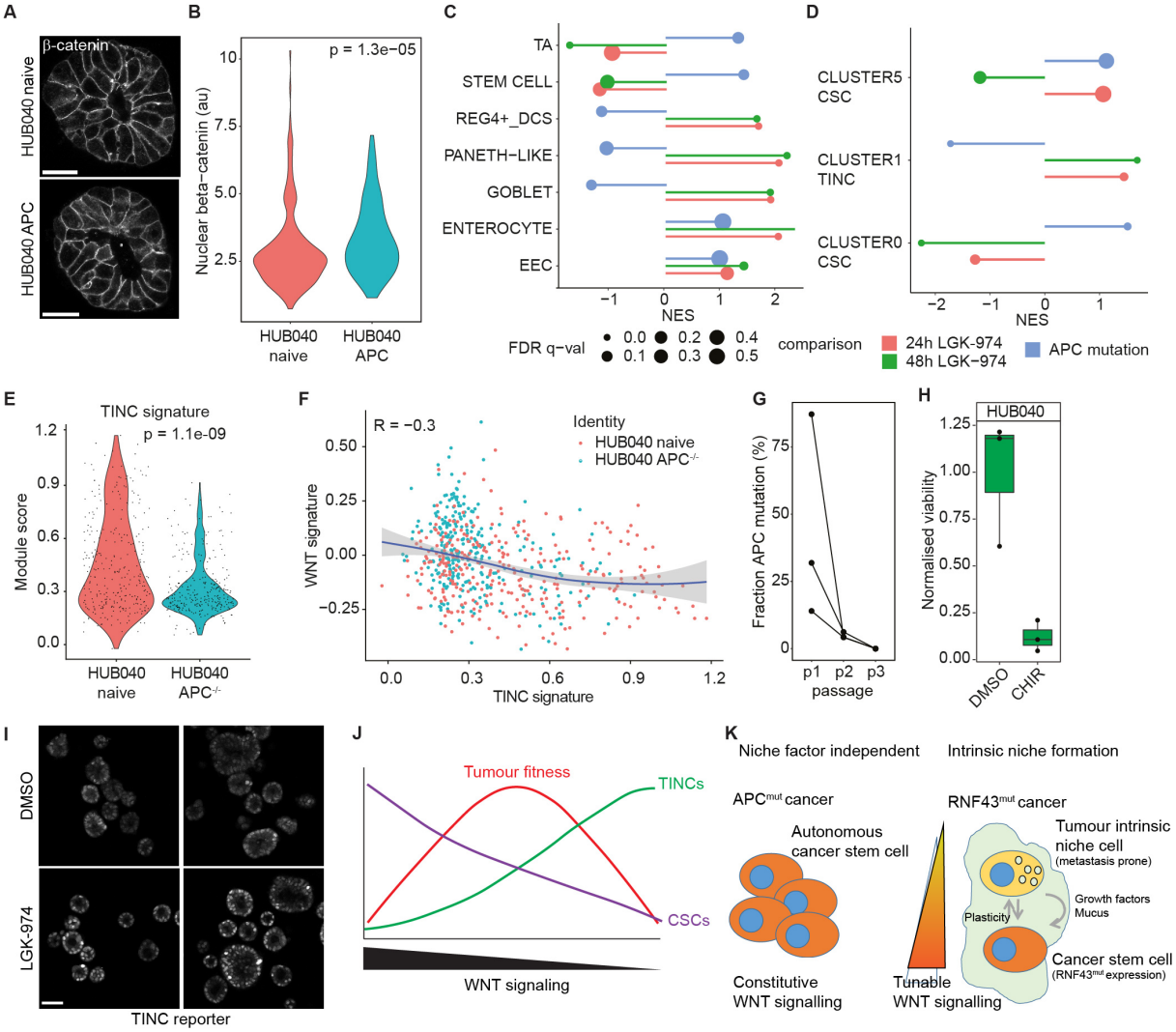

Figure 6 | A tight window of WNT signalling balances tumour niche cells and stem cells. **A.** Representative confocal microscopy pictures of organoids with IF labelling for β-catenin. Scale bar = 20 µm. **B.** Violin plot showing quantification of nuclear β-catenin signal for 205-231 cells per organoid line. **C, d.** Results of GSEA analysis comparing HUB040$^{APC-/-}$ with HUB040 (WNT activation, blue) and HUB040 treated with 100 nM LGK-974 for 24 or 48 hours with DMSO treatment (WNT inhibition, orange and green) by gene signatures of colon-

specific cell types[18,19] (**C**) or HUB040-specific clusters as determined in Figure 3a (**D**). x-axis shows the normalized enrichment score (NES) and size of the dots shows the false discovery rate (FDR). **E.** Violin plots showing single cell module scores for expression of genes from the HUB040 TINC signature grouped by organoid line of origin. **F.** Scatter plot showing inverse relation between single cell module scores for expression of genes from the HUB040 TINC signature and the Van der Flier WNT signature[52]. Colour of dots indicates line of origin. **G.** Line graph showing fraction of *APC* mutant DNA after each passage in the competition assay of indicated lines. n = 3. **H.** Box plots showing the relative viability of HUB040 organoids after 14 days treatment with 5 µM CHIR99021 or DMSO control. n = 3 per condition. **I.** Representative confocal microscopy images of HUB040 NDRG1-IRES-mNeon (TINC reporter) organoids after three days treatment with LGK-974 or DMSO control. Scale bar = 50 µm. **J.** Schematic representation of the optimal window of WNT-signalling for fitness of colorectal mucinous adenocarcinomas. **K.** Diagram of the biological model presented in the discussion comparing two routes towards of niche-independency in cancer.

Methods

Patient material

The collection of colorectal tissue for the generation of healthy colon and CRC organoids was performed according to the guidelines of the European Network of Research Ethics Committees (EUREC) following European, national and local law. In all cases, patients signed informed consent after ethical committees approved the study protocols. Organoids identified by HUB codes *HUB-02-B2-040* (HUB040, CRC) and *HUB-02-A2-040* (HUB040N, normal colon) are catalogued at https://huborganoids.nl/ and can be requested at info@huborganoids.nl. Distribution to third (academic or commercial) parties will have to be authorized by the Biobank Research Ethics Committee of the University Medical Center Utrecht (TCBio) at request of Hubrecht Organoid Technology (HUB). P26T (CRC) was established in a previous study.[13]

Organoid culture

Healthy colon organoids and CRC organoids were cultured according to previous protocols[13]. In short, organoids were cultured in drops of Matrigel (Corning) or BME (R&D systems), and the medium was refreshed every two or three days. CRC organoids were passaged using TrypLE Express (Life Technologies) incubation at 37 °C. Healthy colon organoid were passaged using mechanical shearing (pipetting). Healthy colon organoids were cultured in advanced DMEM/F12 medium (Invitrogen), supplemented with 1% Penicillin/Streptomycin (P/S, Lonza), 1% Hepes buffer (Invitrogen), 1% Glutamax (Invitrogen), 1x B27 (Invitrogen), 10 mM Nicotinamide (Sigma-Aldrich), 1.25 mM N-acetylcysteine (Sigma-Aldrich), 50 ng/mL EGF (PeproTech), 500 nM TGF-b type I receptor inhibitor A83-01 (Tocris), 10 µM P38 inhibitor SB202190 (Sigma-Aldrich), 50% Wnt3a-CM (homemade) or 1% surrogate WNT-CM (homemade)[53], 10% Noggin-CM (homemade), 20% Rspo1-CM (homemade) and 100 µg/mL

Primocin (Invitrogen) (full medium). Colorectal carcinoma organoids were cultured in medium without EGF, WNT and RSPO (CRC medium), unless stated otherwise. *RNF43*-corrected (RC), non-corrected (NC) HUB040 clones were maintained in full HCO medium to prevent negative selection against growth factor dependence.

CRISPR strategy and design

To correct the *RNF43* P441fs mutation back to wildtype, HUB040 organoids were electroporated with a single stranded HDR template (ss-oligo) and Cas9-gRNA. The ss-oligo was designed according to previously established optimal rules.[54,55] Briefly, the *RNF43* mutation in HUB040 is a five base pair duplication, which was corrected in the template. The template was an asymmetric template oligo complementary to the non-target strand overlapping the Cas9 cut site with 36 bp extension on the PAM-distal side, and with a 91-bp extension on the PAM-proximal side of the break. The ss-oligo was ordered at Integrated DNA Technologies with phosphorothioate modifications of the last two nucleotide bonds at the 3' and 5' end (sequence: TATGCACAAGGCTGGGGAATGAGCCACCTCCAATCCACCTCACAGCACCCTGCTGCTTGCCCAGTGCCCCTACGCCGGGCCAGGCCTCCAGACAGCAGTGGATCTGGAGAAAGCTATTGCACAGAACGC). A gRNA was chosen using the Benchling tool (https://benchling.com) that created a double stranded break close to the mutation (sequence: CCAGATCCACTGCTGTCAGG) and cloned in pSpCas9(BB)-2A-Puro (Addgene, 48139).

APC mutations were introduced by targeting the mutation cluster region (MCR) in the *APC* gene using previously reported gRNA (sequence: TACATCTGCTAAACATGAG).[31]

Reporter targeting vector was generated by altering *HR180-LGR5-iCT* plasmid (Addgene #129094) into a plasmid compatible with insertion of homology arms using golden-gate

cloning[56]. iCaspase-T2A-tdTomato sequence was removed and swapped for mNeonGreen-NLS using a combination of Q5® High-Fidelity DNA Polymerase and the In-Fusion HD Cloning kit (Takara). Final targeting vector was generated by insertion of homology arms (~600bp each) flanking the targeted region downstream of NDRG1 to obtain the NDRG1-specific *IRES-mNeonGreen-NLS-WPRE-bGHpA-EF1-Ruby-T2A-Puro-SV40pA* targeting plasmid. gRNAs were cloned into pSpCas9(BB)-2A-Puro using golden gate cloning (sequence: CCGGACTCTGATCTCTGTAG)).)).

Electroporation

Organoid electroporation was performed as previously described[57]. Briefly, organoids were grown in antibiotic-free medium including 10 µM Y-27632 (Selleck chemicals) for two days before electroporation. 24 hours before electroporation, 1.25% DMSO was added to the culture medium. For electroporation, the NEPA21 electroporator was used with the configuration reported by Fujii et al.[57]. For *RNF43* correction and generation of TINC-reporter, 5 µg of Cas9-gRNA and 5 µg template were transfected. For other CRISPR targeting, 10 µg of Cas9-gRNA was transfected. Organoids were recovered for two days by adding medium supplemented with 10 µM Y-27632. From five days post-electroporation organoids were grown in full medium. For CRISPR-engineered organoids, single clones were established by manual picking of individual organoids derived from single cells and genotyped. Reporter lines were selected by puromycin treatment and sorted for the constitutive mRuby fluorophore and single cell derived clones were picked manually and genotyped.

Genotyping

For genotyping of genome-edited organoids, genomic DNA was isolated using QIAamp DNA micro kit (Qiagen). PCR amplification performed using using GoTaq Flexi DNA polymerase (Promega) and products were loaded on an agarose gel. Gel fragments of expected sizes were isolated using QIAquick gel extraction kit (Qiagen) and sequenced by Sanger sequencing. Knockout and Knockin efficiencies were determined using the TIDE[58] (http://shinyapps.datacurators.nl/tide/) and TIDER[59] (http://shinyapps.datacurators.nl/tider/) tools respectively. Manual verification of genotypes for clonal lines was done in Benchling.

HUB040 NDRG1-IRES-mNeon clonal organoid lines were genotyped to confirm homozygous integration of the knock-in construct using gel electrophoresis of PCR products.

Primers used for genotyping are listed in Supplementary Table 1.

Whole-Genome Sequencing and mapping

Genomic DNA of naïve HUB040 and clonal organoid lines was isolated using QIAamp DNA micro kit (Qiagen) and DNA libraries for Illumina sequencing were generated by using standard protocols (Illumina) Libraries were sequenced on a NovaSeq 6000 S4 platform with 2 x 150 bp read length to 30 times base coverage.

Sequencing reads were mapped against human reference genome GRCh38 by using Burrows-Wheeler Aligner v0.7.17 mapping tool[60] with settings 'bwa mem -c 100 -M'. Sequence reads were marked for duplicates by using Sambamba[61] v0.6.8 and sequence read quality scores were recalibrated with GATK[62] BaseRecalibrator v2.7.2. CNVs detection was performed with Control-FREEC[63] v11.56. Full pipeline description and settings are also available at: https://github.com/UMCUGenetics/IAP.

Mutation calling and filtering

Mutation calling and filtering was performed on multi-sample vcfs generated by IAP using HaplotypeCaller from GATK v.4.1.3.0. GATK's VariantFiltration was used for variant quality evaluation with options: "--filter-expression 'QD < 2.0' --filter-expression 'MQ < 40.0' --filter-expression 'FS > 60.0' --filter-expression 'HaplotypeScore > 13.0' --filter-expression 'MQRankSum < -12.5' --filter-expression 'ReadPosRankSum < -8.0' --filter-expression 'MQ0 >= 4 && ((MQ0 / (1.0 * DP)) > 0.1)' --filter-expression 'DP < 5' --filter-expression 'QUAL < 30' --filter-expression 'QUAL >= 30.0 && QUAL < 50.0' --filter-expression 'SOR > 4.0' --filter-name 'SNP_LowQualityDepth' --filter-name 'SNP_MappingQuality' --filter-name 'SNP_StrandBias' --filter-name 'SNP_HaplotypeScoreHigh' --filter-name 'SNP_MQRankSumLow' --filter-name 'SNP_ReadPosRankSumLow' --filter-name 'SNP_HardToValidate' --filter-name 'SNP_LowCoverage' --filter-name 'SNP_VeryLowQual' --filter-name 'SNP_LowQual' --filter-name 'SNP_SOR' -cluster 3 -window 10".

Subsequently, SNPEffFilter[64], SNPSiftDbnsfp (database dbNSFP3.2a[65];, GATK VariantAnnotator (database COSMIC v.89), and SNPSiftAnnotate (database GoNL release 5) were used for variant annotation.

Finally, to obtain catalogues of high-quality somatic mutation calls, we applied post-processing filtering steps, per sample, as described below (all scripts are available at: https://github.com/ToolsVanBox/SMuRF).

Briefly, only variants were considered if present on autosomal chromosomes, passed VariantFiltration with a GATK phred-scaled quality score ≥ 100, had a base coverage of at least 10X, had a mapping quality (MQ) score of 60, did no overlap with single nucleotide polymorphisms (SNPs) in the Single Nucleotide Polymorphism Database v146 and a panel of unmatched normal human MSC and fetal genomes (BED-file available upon request), had a

GATK genotype score (GQ) of 99 (indel/sbs in clonal sample, or indel in paired control) or higher than 10 (sbs in paired control), had a variant allele frequency (VAF) of >=0.1 to exclude *in vitro* accumulated mutations.

Identification of driver mutations

Single base substitutions or indels were considered as driver mutations when they have a MQ of 30, a minimal base coverage of 10x, had a VAF equal or higher than 0.1, or present in driver genes COSMIC cancer gene consensus (version of 9/5/2019), were also annotated as missense, frameshift, stop-gain, insertion or deletion, had either a high or moderate expected effect as annotated by SnpEff, and were not present in the Single Nucleotide Polymorphism Database v146 and a panel of unmatched normal human MSC and fetal genomes (BED-file available upon request). Oncoplot (Figure S1A) was generated with the ComplexHeatmap[66] v2.12.0 package from Bioconductor.

Structural variant and chromosomal copy-number alteration calling was performed using the GRIDSS-purple-linx[67] pipeline developed at the Hartwig Medical Foundation.

***In vivo* subcutaneous tumorigenesis**

Animal experiments were approved by the Competent Authority, The Netherlands (License number AVD115002016614), which is advised by the Animal Ethics Committee. Animal work protocol (614-1-22) was approved by the Animal Welfare Body and were performed in accordance with the Dutch Law on Animal Experiments and the European Directive 2010/63/EU. Healthy 8–10 week old 25–30 g male *NOD.Cg-Prkdc*^{scid} *Il2rg*^{tm1Wjl}*/SzJ* (NSG) mice were supplied by Charles River. Animals were randomly allocated in groups of three mice

into individually ventilated cages. Animals were kept at room temperature under 12 hours light/dark cycles and received standard chow pellets and water ad libitum. HUB040 organoids were dissociated five days after passaging into single-cells by TrypLE Express incubation for 5 min at 37 °C. A cell-matrigel (1:1) suspension was prepared with 5×10^6 cells/mL. Using a 1 mL syringe and 25G 0.5 × 16 mm needles, 100 µl of the suspension were subcutaneously injected into the right flank of animals. Animal welfare was monitored by physical appearance, behaviour, and body weight. Animals were sacrificed when the tumour volume (V) reached 1.5 mm^3, as measured by $V = 1/2 \times (\text{smaller diameter}^2 \times \text{larger diameter})$. Tumour tissue was harvested for further immunohistochemical analyses. Sample sizes are outlined in the figure legends. Mice were randomly assigned to experimental groups. No blinding method was used for injection. No animals were excluded from downstream analysis.

Orthotopic implantation in the caecum of NSG mice

In order to evaluate the tumourigenic capacity of the organoids, murine orthotopic caecum-implantation model[17] was used as described in animal work protocol (614-1-22). In summary, day before implantation, HUB040 organoids were dissociated into single cells and 2.5×10^5 cells were plated in 10 µL drops of neutralized Rat Tail High Concentrated Type I Collagen (Corning, C3867). Cultures were allowed to recover overnight at 37 °C, 5% (vol/vol) CO2. NSG mice were treated with a s.c. dose of Carprofen (5 mg/kg, Rimadyl™) 30 min before surgery and were subsequently sedated by using isoflurane inhalation anesthesia [~2% (vol/vol) isoflurane/O2 mixture]. The caecum was exteriorized through a midline abdominal incision and a single collagen drop containing organoids was surgically transplanted in the cecal submucosa. Carprofen was administrated s.c. post 24 hour surgery. Animal welfare was monitored by physical appearance, behaviour, and body weight. Power analyses were carried

out prior to experiments being carried out to determine the minimum number of animals required for each experiment. These analyses were informed by previous and / or preliminary experiments. Animals were house vested in groups of four. Every group (i.e. cage) contained mixture of mice transplanted with both organoid genotypes. No animals were excluded from downstream analysis. The biotechnician was blinded to the group allocation of the animals during the experiment.

Immunohistochemistry (IHC)

Mouse tissues with or without organoid-initiated tumours/metastases were fixed in 4% formaldehyde solution and paraffin embedded. Sections of 4 µm thickness were made. Prior to the staining, tissue sections were deparaffinized and rehydrated. Endogenous peroxidase activity was blocked with 1.5% hydrogen peroxide for 30 min. Heat-induced antigen retrieval was carried out using citrate buffer pH6.0 for 20 min, followed by the cooling of tissue sections for 20 min. Sections were incubated overnight at 4 °C with primary antibodies (anti-hNucleoli clone NM95, Abcam (ab190710) 1:1000 and anti-Mucin2 clone (H-300), Santa Cruz (sc-15334), 1:100) diluted in PBS with 0.1% Sodium azide and 3% BSA. The next day, sections were washed three times with 0.05% Tween-PBS solution for 5 min, followed by a 1 hour incubation with the HRP-conjugated secondary antibody. Subsequently, sections were washed three times with 1× PBS for 5 min and developed with 3,3'-Diaminobenzidine (DAB) chromogen for 10 min at room temperature in the dark. Sections were rinsed under running tap water for 10 min and counterstained with hematoxylin, followed by dehydration and mounting.

Stainings were scanned using NanoZoomerXR whole slide scanner (Hamamatsu) at 40X magnification, with a resolution of 0.25 µm/pixel. Quantification of the scans was performed using QuPath program analysis program[68]. Target of interest (tumour or distinct

immune populations) was quantified using QuPath's Trained Pixel classification command that allows an automated recognition of background, tissue (hematoxylin) and DAB staining areas. The percentage of target of interest area was then calculated by using the following formula: DAB area / (DAB + tissue– background area) * 100.

Reconstitution assays using growth factor and drug treatments

Single cells from organoid were harvested using TrypLE incubation at 37 °C. Cells were filtered through a 40 µm nylon cell strainer (Falcon). Cells were counted and seeded in a $1*10^6$ cells / mL dilution in Matrigel/BME. Cultures were incubated in standard culture medium with indicated additions/depletions of factors and drugs, which was replenished every 2-3 days. After seven days, brightfield images were taken using an EVOS imaging system and organoids were split 1:2 similar as mentioned before, after which outgrowth was monitored again for seven days. Quantitative viability assays were performed by CellTiter-Glo® (Promega) or Alamar Blue® (Thermo Fisher) according to manufacturer instructions. Pictures are shown for a representative experiment, which was performed at least three times. Normalized viability data was combined from multiple experiments and two or three technical replicates per experiment.

Bulk RNA sequencing

Organoids were lysed in RLT lysis buffer (Qiagen) + 1% β-mercapto-ethanol; seven days after passaging. Biological triplicates were employed that were passaged and lysed at separate moments. For the LGK-974 experiments, organoids were treated with 100 nM LGK-974 or a DMSO volume control for 24 or 48 hours prior to lysis. RNA was obtained using the Qiagen QiaSymphony SP (Qiagen) according to the manufacturer's protocol. Library prep was performed using Truseq RNA stranded polyA (Illumina). Libraries were sequenced on an

Illumina NextSeq2000 platform with 1x50bp reads. Single-end RNASeq reads were processed using the UMCU RNASeq pipeline (v2.3.0) with default settings. Read quality was assessed by FastQC (0.11.4) followed by splice-aware alignment against the human reference genome (GRCh38) with STAR[69] (2.4.2a). RNA expression quantification was performed with htseq-count (0.6.0) in reverse-stranded mode. Differential gene expression analysis was performed with the DESeq2[70] (1.22.2) R package. In each comparison, genes were selected with an absolute fold-change > 1.5 and p adjusted < 0.05. Generation of heatmaps and scatterplots was done in using the pHeatmap and ggplot2 R packages.

GSEA and gene signatures

Gene set enrichment analyses (GSEA) were performed using the Broad Institute GSEA tool (software.broadinstitute.org/gsea/index.jsp) with default settings, including permutation by gene sets. HALLMARK genesets were derived from the Molecular Signatures Database.[71] Geneset for REG4$^+$ deep crypt secretory cells (DCSs) was defined as human orthologues (identified by bioDBnet) of the >2 fold upregulated genes with a p-value < 0.05 in Reg$^+$ cells compared to Lgr5$^+$ cells that were previously reported.[18] Gene sets for human colon specific cell types were derived from a published single-cell transcriptome study (Wang et al. table S2).[19] Genesets for HUB040 single cell clusters were defined by marker gene analysis using the 'FindAllMarkers' command in Seurat comparing one cluster to all other clusters using a wilcox test. Threshold for adjusted p-value was set at p < 0.05. The WNT signature was reported previously by Van der Flier *et al.*[52]

For the analysis of secretory genes, a list of secreted proteins was downloaded from human protein atlas ("Secreted proteins predicted by MDSEC")[72]. Downregulated secretory genes

were defined as: significantly downregulated in at least three comparisons and not upregulated in the other comparison (RC1 vs HUB040, RC2 vs HUB040, RC1 vs NC1, RC2 vs NC1)

Single cell RNA sequencing and analysis

Single cells from organoid were harvested using TrypLE incubation at 37 °C, seven days after passaging. Cells were filtered through a 40 µm nylon cell strainer (Falcon). scRNA-seq was performed according to the Sort-seq protocol[73]. Libraries were sequenced on an Illumina NextSeq500 at paired-end 60- and 26-bp read length and 75,000 reads per cell.

Reads were mapped to the hg38 reference genome. Analysis was performed with the R-package Seurat[74] (4.0.4). Cells with 400-50000 unique features and 1000-7000 total transcript counts were included in the analysis. Scores for gene signature expression were calculated using the AddModuleScore function.

Signature enrichment in marker gene lists was determined using the Enrichr tool[75] (https://maayanlab.cloud/Enrichr/).

To analyse fraction of TINCs in *RNF43*-corrected and non-corrected clones, cells were filtered according to previously mentioned settings and for each cell a module score for the original TINC signature was calculated. Cells with a module score > 0.61 were scored as TINC, which corresponded to 16% of cells in the HUB040 naïve sample (which was the fraction of cells mapping to cluster 1 in the original analysis). Data was plotted using ggplot2.

To validate the TINC signature in a human cohort, published RNAseq data of tumour epithelial cells of colorectal cancer patients were used[6]. Twenty *RNF43* wildtype patients from iCMS2 cohort based on single-cell RNA sequencing and inferred CNV result and four *RNF43* mutant patients were selected. After selecting patients, supervised clustering using 154 TINC signature

genes was performed with batch correction using harmony algorithm[76] to remove patient specificity. Differential gene expression analysis was performed using the 'FindAllMarkers' command in Seurat with logistic regression framework.

TCGA data analysis

Signature scores for indicated gene sets were calculated for each samples as log2 Z-score over the total TCGA Colon Adenocarcinoma set (rpkm values of 382 samples - cbcoad) using the R2 genomic analysis platform (http://r2.amc.nl). TINC signature was determined as the top 25 marker genes for cluster 1 in HUB040 (from Seurat marker gene analysis). *RNF43* mutation status was determined by combining the list of *RNF43* mutant TCGA samples (derived from C-bioportal) combined with results of re-analysis by Gianakkis *et al.*[32] calling additional mutations that were falsely labelled as polymerase slipping errors in the original TCGA analysis.[32] CMS classifications were derived from the Colorectal Cancer Subtyping Consortium (CRCSC)[77], samples without CMS label have been left out of the analysis. Classification as mucinous was derived from Cancer Type in cbioportal (mucinous adenocarcinoma of colon and rectum). "High and low WNT" was defined as the upper and lower quartile of the Z-scores for the intestinal WNT/TCF signature as reported by Van der Flier *et al.*[52].

Immunofluorescence

For staining of Mucin2, organoids were seeded in 15-well IBIDI angiogenesis chambers during passaging and fixed 7-12 days later in 4% paraformaldehyde (PFA) (Sigma-Aldrich) for 60 min at room temperature. The fixation was quenched using 0.05 M NH_4Cl and cells were permeabilised with PBD0.2T (48,5mL PBS, 1mL 10%Triton, 0,5mL DMSO and 0,5g BSA) for 20 min at room temperature. The organoids were incubated with primary antibodies diluted

in PBD0.2T at 4 °C overnight. Washes were performed with PBD0.2T after which secondary antibodies were incubated for 3h at room temperature. Stained organoids were mounted using IBIDI mounting medium.

For other stainings, organoids were cultured as usual. 7-12 days after passaging, matrix was removed using dispase (Invitrogen) and organoids were transferred to 8-well IBIDI imaging slide. Fixation, permeabilisation and antibody staining were performed inside the imaging slide, as indicated above, except for primary antibody incubations were performed for one hour at room temperature. Stained organoids were mounted using IBIDI mounting medium.

The following antibodies and dyes have been used for immunofluorescence: Mouse-anti-Mucin2 (sc-515032, Santa Cruz, 1:200), Mouse-anti-β-catenin (610154, BD Transduction Laboratories, 1:200), Rabbit-anti-KI67 (ab15580, Abcam, 1:200), Goat-anti-Mouse-Alexa-488 (A11029, Invitrogen, 1:600) Goat-anti-Rabbit-Alexa-647 (A21245, Invitrogen, 1:600), Phalloidin-Alexa-647 (8940S, CST, 1:200) and Dapi (D9542, Sigma, 1:1.000). Images were acquired with a Zeiss LSM700 confocal microscope.

Image processing was performed using FIJI (2.3.0). Nuclear β-catenin and TINC-reporter intensity were quantified using the StarDist plugin (0.8.3)[78] with the Dapi staining used for single nucleus segmentation. Data was analysed and plotted in R.

Hybrid organoid co-culture, time-lapse imaging and analysis

The protocol on generating hybrid organoid co-cultures has been described previously[20]. In short: HUB040 naïve organoids were transduced with mCherry tagged H2B constructs and HUB040 RC2 organoids with mNeon green tagged H2B constructs and selected by FACS sorting. Six days post splitting, both lines were starved in CRC medium for 24 hours and at day 7 broken up into small clumps of cells that were mixed in 1:1 ratio. Cells were concentrated by

centrifugation, resuspended in a small volume of CRC medium and incubated at 37 °C for 30 min Cell aggregates were plated in 10 µL BME droplets in an 18 Well µ-Slide (IBIDI #81811). Three days after plating, time-lapse microscopy was performed on an inverted LSM880 Fast AiryScan scanning confocal microscope (Zeiss) using LSM scanning mode with a 488nm Argon-laser and 561nm Diode-laser, equipped with a 20X dry immersion objective (Objective Plan-Apochromat 20x/0.8 M27, Zeiss). Cells were kept in CRC medium at 37°C under 5% CO2 for the full duration of the experiment. Images were acquired with a Z-interval of 5µm covering the full volume of the organoid and time-interval of one hour for a total duration on 60 hours. Time-lapse images were processed and analysed following a previously described pipeline in which depth-encoded movies were generated in which cell divisions and cell dead events were scored[79]. The cell death / mitosis ratio was calculated as a proxy for organoid survival. Cell numbers at the start of time-lapse were counted using Imaris software (Andor version 9.9.1). Videos and snapshots of 3D-reconstructed representative organoids were made in Imaris.

Flow cytometry analysis and sorting of organoids

Single cells from organoid were harvested using TrypLE incubation at 37 °C. Cells were filtered through a 40 µm nylon cell strainer (Falcon) and live-cells were measured at a FACS Celesta with FACS Diva software (BD). The following fluorescent channels were used: BB515 for mNeon, PE-CF594 for mRuby and PE-Cy5 for Alexa-647 labelled Edu.

EdU incorporation assays were performed by culturing organoids in CRC medium containing 10 µM EdU for 16 hours to cells, after which single cells were harvested, fixed in 4% PFA and EdU-labeling was performed according to manufacturer instructions (Click-iT EdU Cell Proliferation Kit for Imaging, Thermo Fisher).

Sorting of TINC-reporter populations was performed using a FACS Aria III machine (BD) Populations were gated for viable single cells which were divided in three equal populations of 20-30% of the total based on mNeon histogram (example in Figure S5A). Sorted cells were directly lysed in RLT lysis buffer (Qiagen) for RNAseq analysis, or taken in culture for organoid reconstitution, by seeding in a $1x10^6$ cells / mL dilution in BME.

Gated single cells were analysed in FlowJo (version 10.6.1).

Western blot

Organoids were collected in Cell Recovery Solution (Corning), incubated for 20 min on ice and subsequently lysed in RIPA buffer containing protease and phosphatase inhibitors. Lysates were boiled in 1x SDS sample buffer and ran on a pre-casted SDS-page gel (Mini protean, BIO-RAD). Gels were transferred to a Immobilon-FL PVDF membranes (Millipore), which was blocked for 1 hour at room temperature in 1:1 ratio Odyssey blocking buffer (LI-COR): PBS, and stained against APC (sc-7930, Santa Cruz, 1:1.000) and Actin (691001, MP, 1:10.000) overnight at 4 °C. Blots were stained with secondary antibodies IRDye-680 goat anti-rabbit (926-32221, LI-COR, 1:10.000) and IRDye-800 goat anti-mouse (925-68070, LI-COR, 1:10.000) for 1 hour at room temperature in the dark. The Typhoon (GE Healthcare) infrared imaging system was used for immunoblot analysis.

RT-qPCR

Organoids, seven days after passaging, or FACS-sorted cell populations were lysed in RLT lysis buffer (Qiagen) + 1% β-mercapto-ethanol and RNA was purified using the RNeasy kit (Qiagen) according to manufacturer's protocol. RNA was used as a template for cDNA

production using the iScript™ cDNA Synthesis Kit (Biorad) according to the manufacturer's protocol. The synthesized cDNA was subsequently used in a qRT–PCR using IQ SYBR green mix (Biorad) according to the manufacturer's protocol. Used primers are listed in Supplementary Table 2

Expression of WNT target genes was corrected against house-keeping gene *GAPDH* and normalized to the control.

APC competition assay

HUB040 and HUB040$^{APC-/-}$ organoids were split into single cells, counted and seeded in a 1:1 ratio. Mixed organoid populations were passaged once a week, and during each passage, genomic DNA was harvested for genotyping the fraction of *APC* mutant alleles as indicated above.

Statistical analyses

For RNA sequencing analysis, statistical significance was determined using the DESeq function in R, which uses a Wald test (two-tailed), see detailed methods. Gene set enrichment was performed as described in the methods. For other data, p values were calculated using the 'stat_compare_means' function of the ggpubr package (0.40.0) in R. For comparing two or more groups of non-parametric data, a two-sample Wilcoxon test or Kruskal-Wallis were used respectively.

Data availability

The scRNA-seq and bulk RNA-seq data generated in this study are available from Gene Expression Omnibus (GEO) under the accession codes GSE213079 (scRNAseq), GSE213077 (bulk RNAseq various organoid lines), GSE212959 (bulk RNAseq RNF43-corrected and non-corrected HUB040 organoids), GSE220128 (bulk RNAseq TINC reporter cells), GSE213068 (bulk RNAseq APC mutant and wildtype HUB040 organoids) and GSE213072 (bulk RNAseq HUB040 organoids treated with LGK-974).

Published scRNA-seq data referenced in the study is available from Synapse under the accession code syn26844071. Published microarray and bulk RNA-seq are available from Gene Expression Omnibus (GEO) under the accession codes GSE41258 and GSE50760, respectively.

Supplementary Information

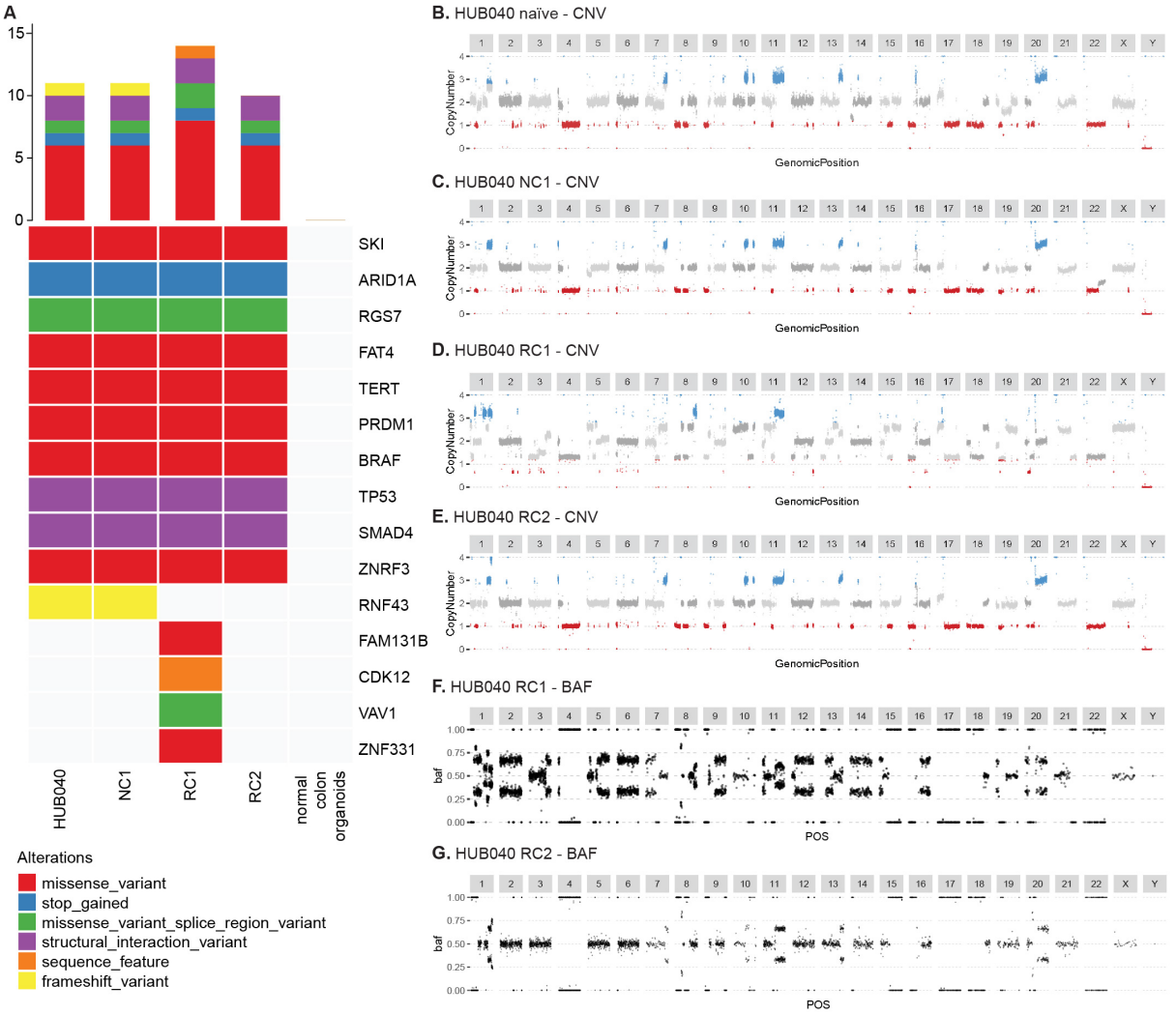

Figure S1 | Whole genome sequencing analyses of HUB040 and clonal organoid lines. A. Oncoplot showing high-confidence putative driver mutations derived from whole genome sequencing data of HUB040, normal colon organoids, NC1, RC1 and RC2. **B-E.** In silico karyograms of HUB040 naïve CRC organoids (**B**), Non-corrected control HUB040 clone (NC1) (**C**), *RNF43*-corrected clone 1 (RC1) (**D**) and *RNF43*-corrected clone 2 (RC2) (**E**). **F, g.** B-allele frequency (BAF) plot for *RNF43*-corrected clone 1 (**F**) and RC2 (**G**) which is indicative of a whole genome duplication event for RC1.

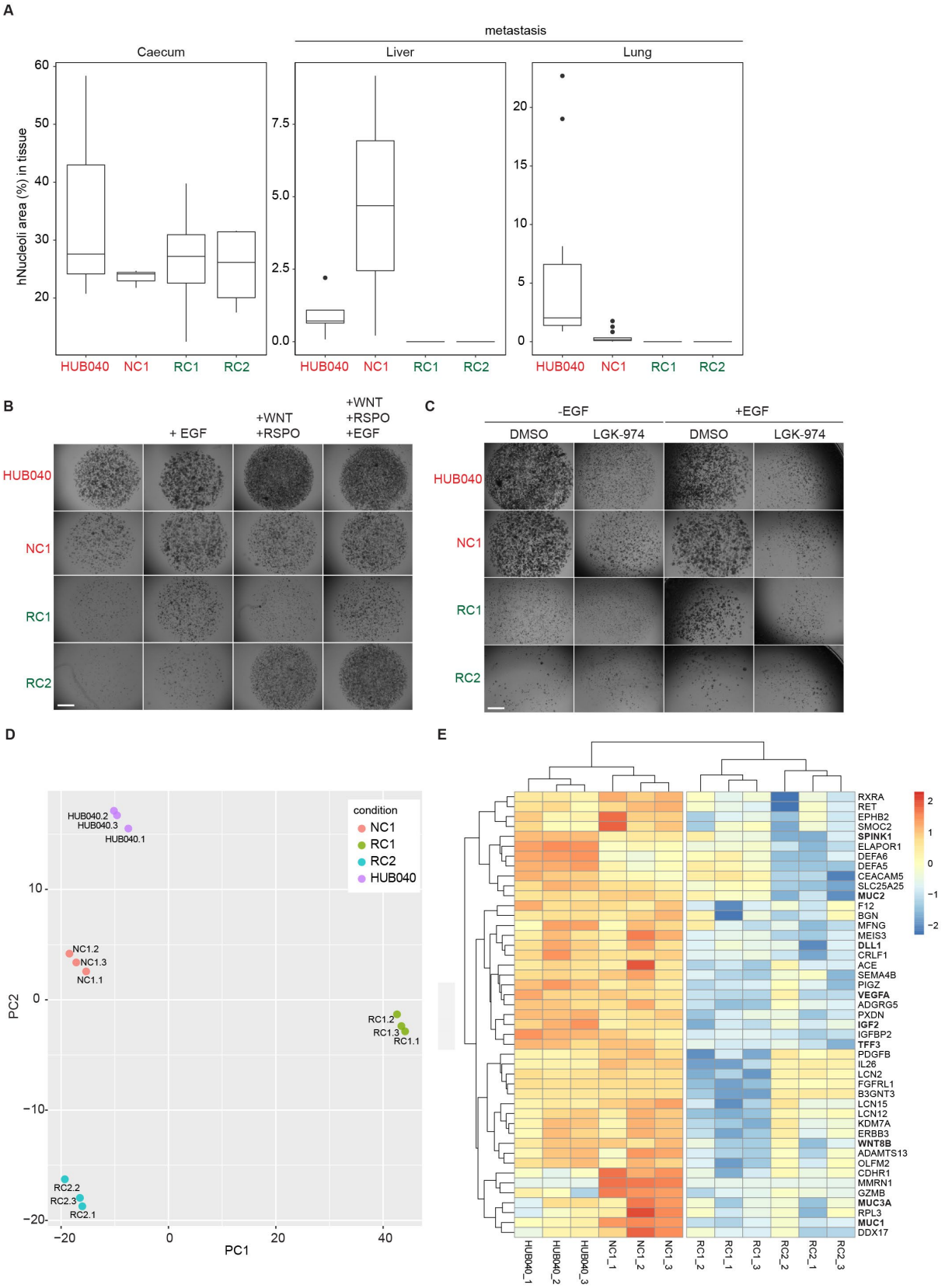
A
metastasis
Caecum
Liver
Lung
hNucleoli area (%) in tissue
HUB040
NC1
RC1
RC2
B
+ EGF
+WNT
+RSPO
+WNT
+RSPO
+EGF
C
-EGF
+EGF
DMSO
LGK-974
D
condition
NC1
RC1
RC2
HUB040
PC1
PC2
E
RXRA
RET
EPHB2
SMOC2
SPINK1
ELAPOR1
DEFA6
DEFA5
CEACAM5
SLC25A25
MUC2
F12
BGN
MFNG
MEIS3
DLL1
CRLF1
ACE
SEMA4B
PIGZ
VEGFA
ADGRG5
PXDN
IGF2
IGFBP2
TFF3
PDGFB
IL26
LCN2
FGFRL1
B3GNT3
LCN15
LCN12
KDM7A
ERBB3
WNT8B
ADAMTS13
OLFM2
CDHR1
MMRN1
GZMB
MUC3A
RPL3
MUC1
DDX17

Figure S2 | RNF43 mutation facilitates niche factor self-sufficiency A. Box plots showing the fraction of tumour tissue relative to total tissue area for caecum, liver and lungs in mice that had a tumour or metastasis (see Figure 2C for statistics). **B.** Representative low-magnification (2x) brightfield images of HUB040-derived clones cultured in CRC medium supplemented with indicated growth factors for 14 days, passaged after 7 days. Scale bar = 1000 µm. **C.** Representative low-magnification brightfield images of indicated HUB040 clones treated with 100 nM PORCN inhibitor LGK-974 or similar volume of DMSO in CRC culture medium with or without EGF supplementation for 14 days, passaged after 7 days. Scale bar = 1000 µm. **D.** Principle component analysis of RNA sequencing data of HUB040 and *RNF43*-corrected and non-corrected clones. **E.** Heatmap of downregulated secretory genes in *RNF43*-corrected HUB040 from a list of 3000+ genes encoding for secreted proteins, as predicted by MDSEC.[72] Coloured bar represents row z-scores of normalised gene counts.

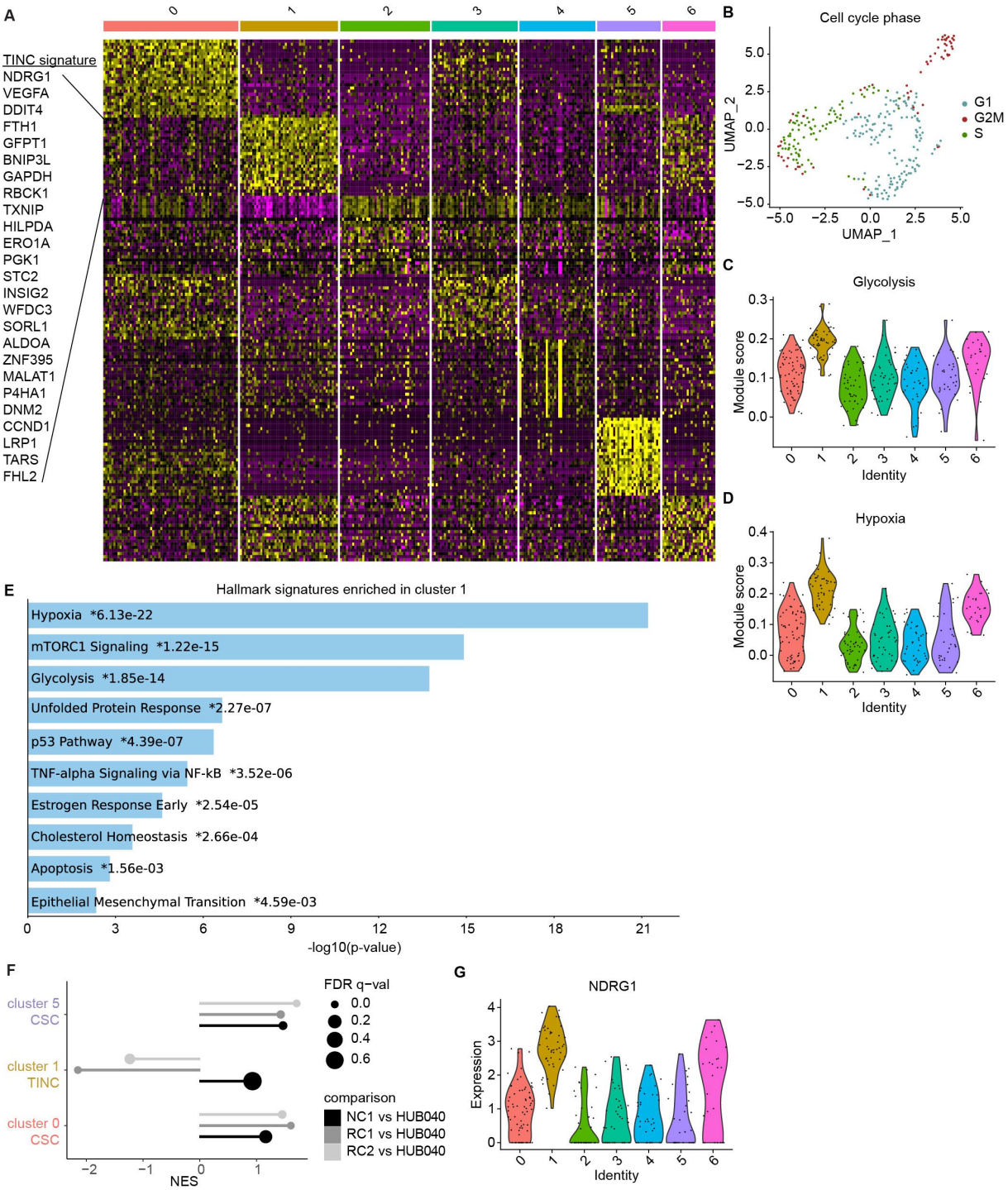

Figure S3 | Supplementary Figures single cell RNAseq HUB040. A. Single cell expression heatmap showing row Z-scores for top 25 marker genes for each cluster. Marker genes for cluster 1 are highlighted and later used as 'TINC signature'. **B.** Reduced dimensionality (UMAP) visualisation with cell cycle phase as determined by Seurat Analysis. **C, D.** Violin plots showing single cell module scores for expression of genes from the HALLMARK

glycolysis (**C**) and hypoxia (**D**) signatures[71] grouped by cluster. **E.** Bar plot showing p-value of the top ten enriched HALLMARK gene signatures in the TINC marker genes list. **F. G.** Results of GSEA comparing *RNF43*-corrected and non-corrected clones with HUB040 naïve by marker gene signatures for three HUB040-specific clusters (CSC clusters 0 and 5 and TINC cluster 1). x-axis shows the normalized enrichment score (NES) and size of the dots represents the false discovery rate (FDR). **H.** Violin plots showing single cell expression levels for NDRG1.

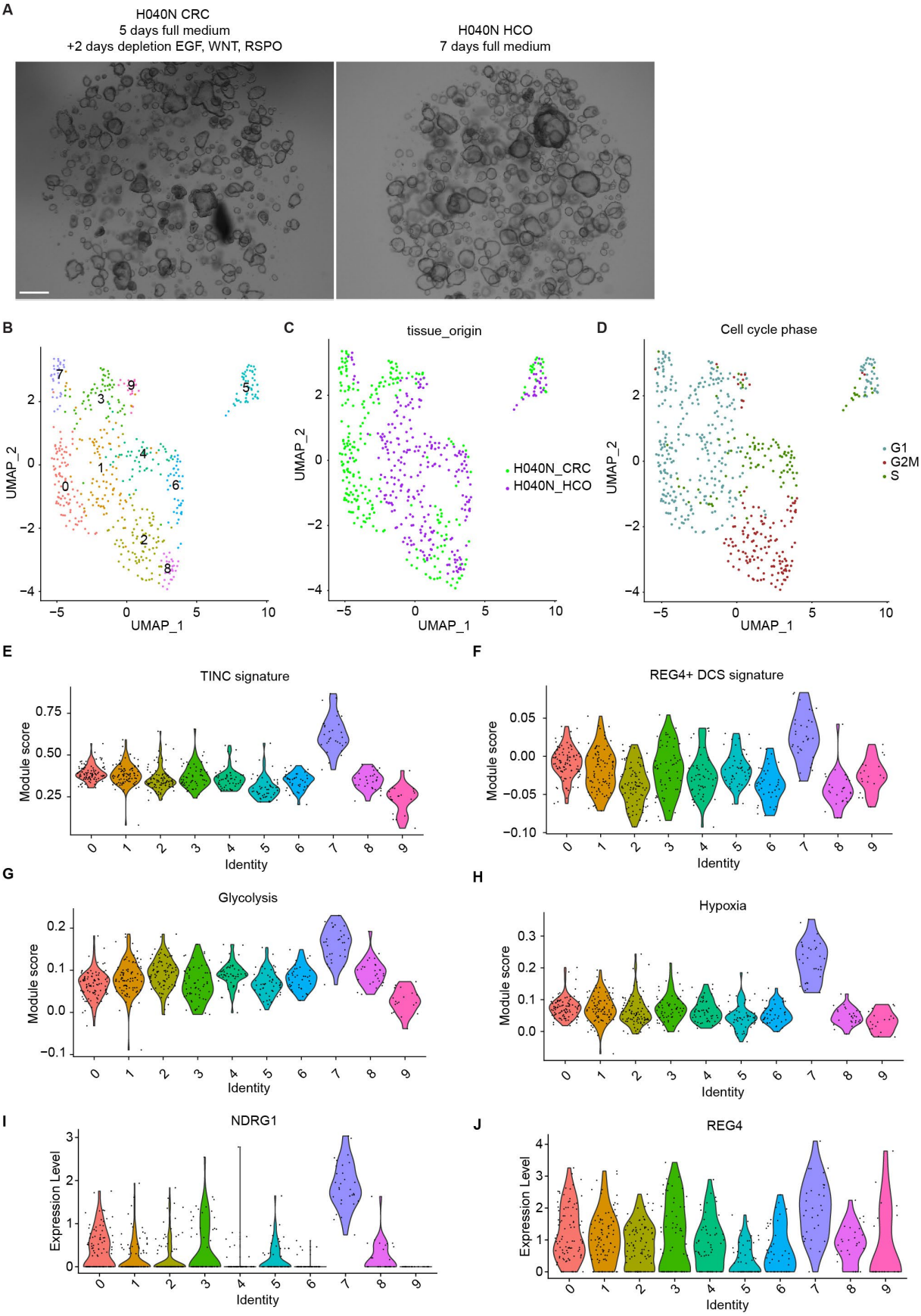
A
H040N CRC
5 days full medium
+2 days depletion EGF, WNT, RSPO
H040N HCO
7 days full medium
B
UMAP_2
UMAP_1
C
tissue_origin
H040N_CRC
H040N_HCO
D
Cell cycle phase
G1
G2M
S
E
TINC signature
Module score
Identity
F
REG4+ DCS signature
G
Glycolysis
H
Hypoxia
I
NDRG1
Expression Level
J
REG4

Figure S4 | Single cell RNAseq normal colon organoids (HUB040N). A. Representative brightfield images of HUB040N normal colon organoid cultures in CRC medium or full (HCO) medium that were used for single cell isolation and sequencing. Scale bar = 1000 µm. **B.** Dimension reduction (UMAP) plot of single cell RNA sequencing data of HUB040N organoids. Results of unsupervised clustering are colour-coded per cluster. **C, D.** UMAP visualisation plotted for tissue of origin (**C**) or cell cycle phase (**D**) plotted. **E-H.** Violin plots showing single cell module scores for expression of genes from the HUB040 TINC (**E**). REG4+ deep crypt secretory cell (DCS)[18] (**F**). HALLMARK glycolysis[71] (**G**) or HALLMARK hypoxia[71] (**H**) signature grouped by cluster. **I, J.** Violin plots showing single cell expression levels for NDRG1 (**I**) and REG4 (**J**).

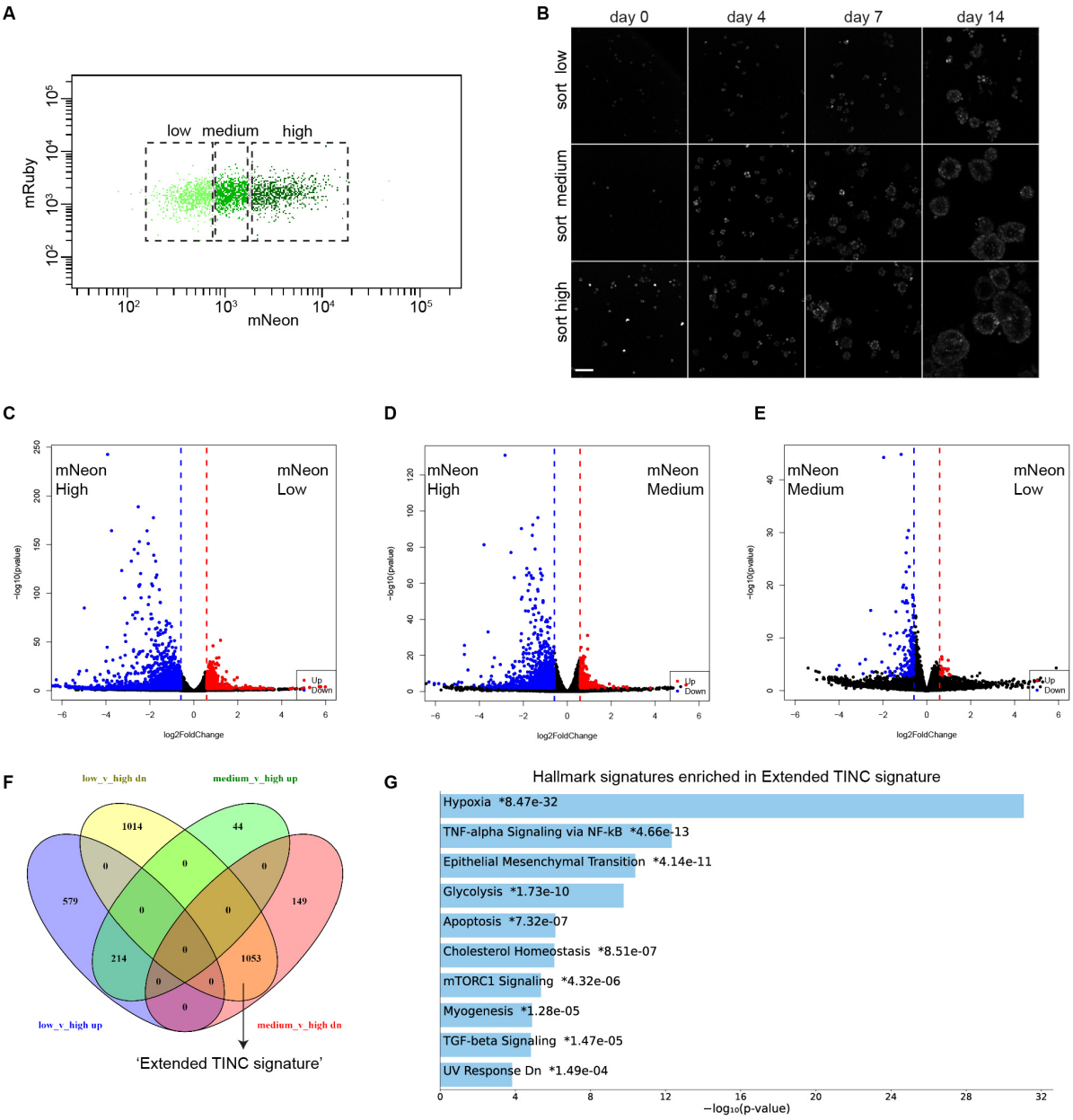

Figure S5 | Supplementary Figures TINC reporter. A. Histogram of mNeon signal for FACS sorted organoid: sorted populations are indicated. **B.** Representative confocal microscopy images of HUB040 NDRG1-IRES-mNeon (TINC reporter) organoids 0, 4, 7 and 14 days after plating of sorted cell populations. Scale bar = 50 µm. **C-E.** Volcano plots of differential gene expression of mNeon-low vs mNeon-high (**C**), mNeon-medium vs mNeon-high (**D**) and mNeon-low vs mNeon-medium (**E**) cells. Significantly (FC > 1.5 and $p < 0.05$) up and down regulated genes are plotted as red and blue dots respectively. **F.** Venn-diagram comparing differentially expressed genes as determined in **C** and **D** and defining and 'Extended TINC

signature' as genes upregulated in mNeon high cells compared to mNeon medium and mNeon low cells. **G.** Bar plot showing p-value of the top ten enriched HALLMARK gene signatures in the Extended TINC signature.

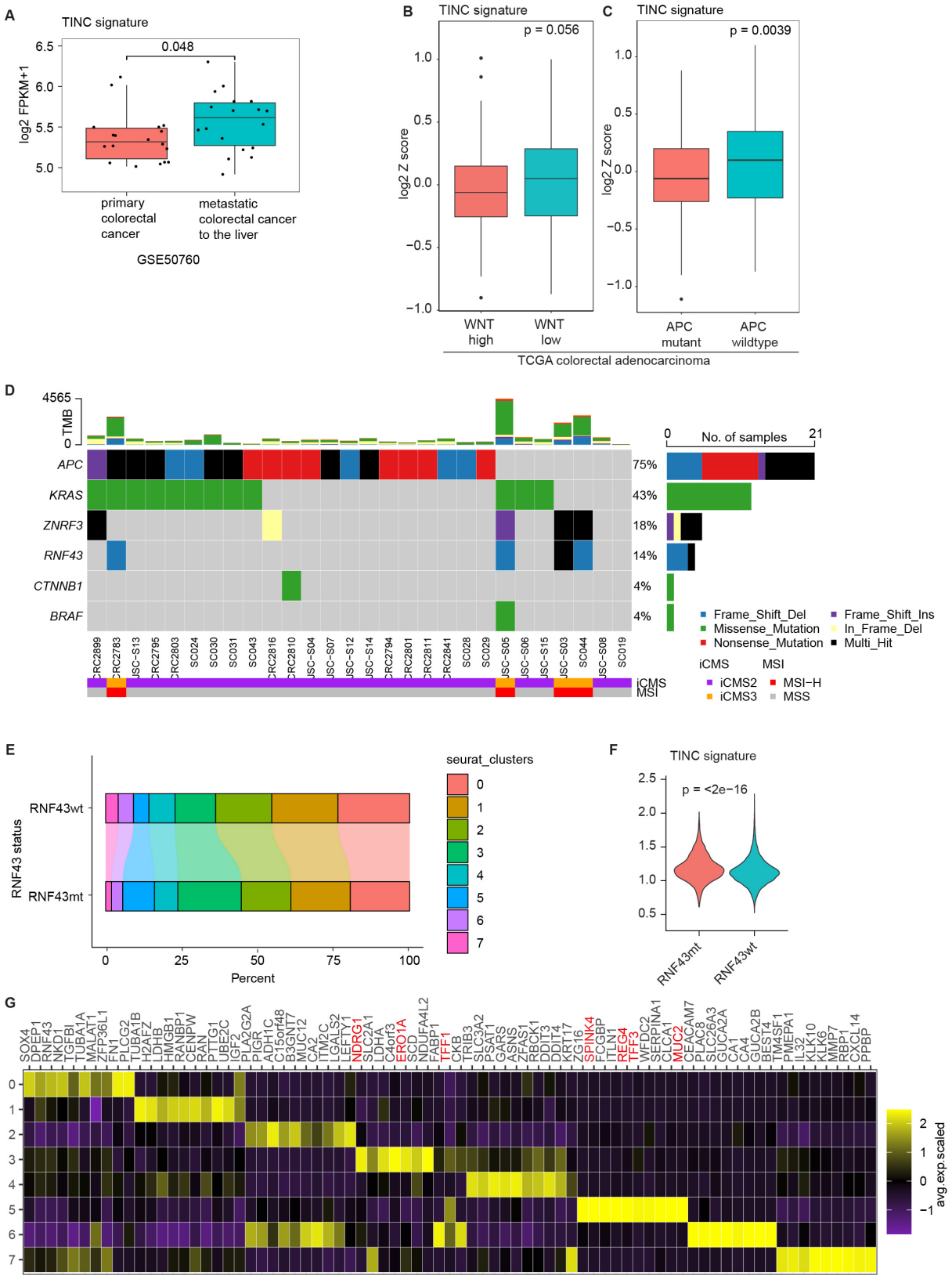

Figure S6 | Supplementary Figure patient data analysis A. Box plots showing expression of TINC signature (log2 FPKM +1) in RNA sequencing data of 18 paired primary colon tumours

and liver metastases[80]. **B, C.** Box plots showing log2 Z-scores for the TINC signature over the colon adenocarcinoma TCGA bulk RNA sequencing dataset grouped by WNT signalling pathway activity as the upper and lower quartile of the Z-scores for the intestinal WNT/TCF signature[52] (n = 95 each) (**B**) or *APC* mutation status (n = 277 mut, 106 wt) (**C**). **D.** Oncoplot showing driver mutation status of the 28 patients included in single cell sequencing cohort[6]. **E.** Alluvial plot comparing the fractions of cells per cluster for *RNF43* wildtype or *RNF43* mutant patient groups. **F.** Violin plots showing single cell module scores for expression of genes from the TINC signature grouped by *RNF43*-mutation status. **G.** Marker gene analysis of the single cell patient data. Genes of interest are coloured red.

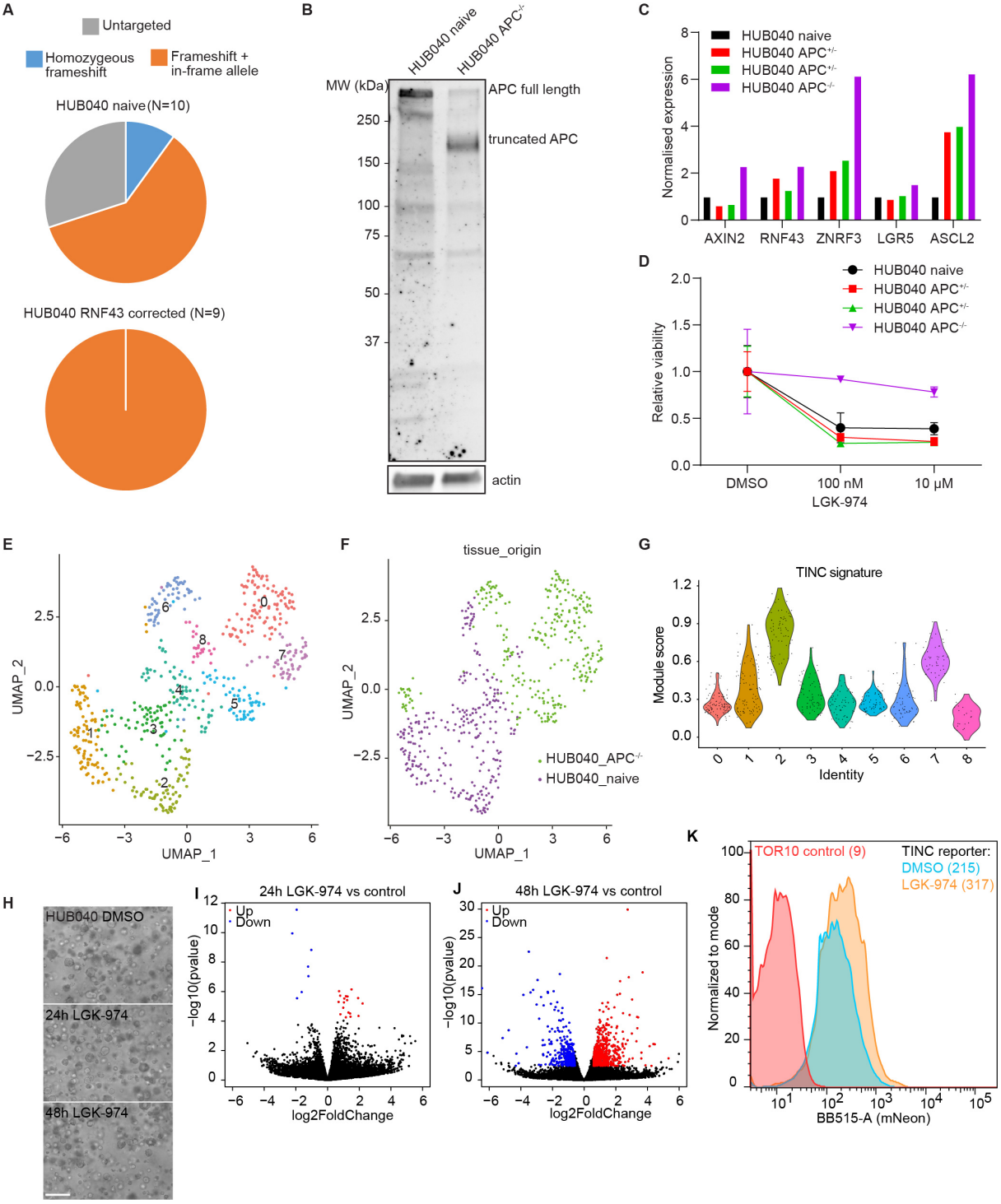

Figure S7 | Supplementary Figure effects APC mutation and LGK-974 on HUB040. A. Pie charts showing the various genotypes found in *APC* targeted single clones of HUB040 and HUB040 RC2 organoids. **B.** Western blot showing truncated APC protein expression in homozygous *APC* mutant HUB040. **C.** Bar plot showing expression values, as measured by RT-qPCR, of classical WNT target genes in HUB040 organoids with CRISPR induced

heterozygous (two clones) or homozygous (one clone) *APC* mutation normalized to naïve HUB040. **D.** Line graph showing relative viability of naïve HUB040 organoids, or HUB040 with heterozygous or homozygous *APC* mutation after seven days treatment with indicated concentration of PORCN-inhibitor LGK-974 or DMSO control. Dots indicate mean and SD. n = 3. **E.** Dimension reduction (UMAP) plot of single cell RNA sequencing data of naïve and *APC* mutant HUB040 organoids. Results of unsupervised clustering are colour-coded per cluster. **F.** UMAP colour-coded per organoid line of origin. **G.** Violin plots showing single cell module scores for expression of genes from the HUB040 TINC signature grouped by cell cluster. **H.** Representative 10x brightfield images of organoid cultures used for RNA isolation. Organoids were treated with 100 µM LGK-974 for 24 or 48 hours, or with vehicle control (DMSO). Scale bar = 200 µm. **I, J.** Volcano plot of differential gene expression between 24h (**I**) or 48h (**J**) LGK-974 treated HUB040 organoid versus DMSO treated HUB040 organoids. Significantly (FC > 1.5 and $p < 0.05$) up and down regulated genes are plotted as red and blue dots respectively. **K.** Histogram showing FACS analysis of HUB040 NDRG1-IRES-mNeon reporter organoids after three days treatment with LGK-974 or DMSO control. Mean fluorescence intensity is indicated.

Supplementary table 1: primers used for genotyping and Sanger sequencing

RNF43_P441_fw	AAATGGCTGAGGGGAGGTTTAG
RNF43_P441_rev	AGGGAGCTGCAGAAAGTAGAAC
APC_fw	TGTAATCAGACGACACAGGAAGCAGA
APC_rev	TGGACCCTCTGAACTGCAGCAT
NDRG1_reporter_internal_fw	GGGCTGTCCCTGATATCAAACAT
NDRG1_reporter_internal_rev	CAGATCCCATACAATGGGGTAC
NDRG1_reporter_upstream_fw	TCTTTGGGAGAGATGACAACGA
NDRG1_reporter_downstream_rev	CCTGCTTTTGCTGCACATTAAG

Supplementary table 2: RT-qPCR primers

GAPDH	CTTTTGCGTCGCCAG	TTGATGGCAACAATATCCAC
AXIN2	AAAGAGAGGAGGTTCAGATG	CTGAGTCTGGGAATTTTTCTTC
RNF43	TGTGTACAAGAACCAAAAGG	CAGGATGATCACAAAGATGG
ZNRF3	CATCCTCCTTGTCAAAATCAAG	TTCTGGTTTCCATCTTCTCTAG
LGR5	AAATGCCTTATGCTTACCAG	ATCTTGAGCCTGAAACATTC
ASCL2	CGTGAAGCTGGTGAACTTGG	GGATGTACTCCACGGCTGAG

Supplementary video 1: Time-lapse series of 3D reconstructed pure RC2 H2B-mNeon organoid in growth factor depleted medium, representative image related to Figures 3I and 3J.

Supplementary video 2: Time-lapse series of 3D reconstructed RC2 H2B-mNeon organoid in hybrid structure with HUB040 H2B-mcherry in growth factor depleted medium, representative image related to Figures 3I and 3J.

References

1. Spit, M., Koo, B.K., and Maurice, M.M. (2018). Tales from the crypt: Intestinal niche signals in tissue renewal, plasticity and cancer. Open Biol. *8*. 10.1098/rsob.180120.

2. Sato, T., Vries, R.G., Snippert, H.J., Wetering, M. Van De, Barker, N., Stange, D.E., Es, J.H. Van, Abo, A., Kujala, P., Peters, P.J., et al. (2009). Single Lgr5 stem cells build crypt – villus structures in vitro without a mesenchymal niche. Nature *459*, 262–266. 10.1038/nature07935.

3. Fumagalli, A., Drost, J., Suijkerbuijk, S.J.E.E., Van Boxtel, R., De Ligt, J., Offerhaus, G.J., Begthel, H., Beerling, E., Tan, E.H., Sansom, O.J., et al. (2017). Genetic dissection of colorectal cancer progression by orthotopic transplantation of engineered cancer organoids. Proc. Natl. Acad. Sci. U. S. A. *114*, E2357–E2364. 10.1073/pnas.1701219114.

4. Fujii, M., Shimokawa, M., Date, S., Takano, A., Matano, M., Nanki, K., Ohta, Y., Toshimitsu, K., Nakazato, Y., Kawasaki, K., et al. (2016). A Colorectal Tumor Organoid Library Demonstrates Progressive Loss of Niche Factor Requirements during Tumorigenesis. Cell Stem Cell *18*, 827–838. 10.1016/j.stem.2016.04.003.

5. Fearon, E.F., and Vogelstein, B. (1989). A Genetic Model for Colorectal Tumorigenesis. *61*, 759–767.

6. Joanito, I., Wirapati, P., Zhao, N., Nawaz, Z., Yeo, G., Lee, F., Eng, C.L.P., Macalinao, D.C., Kahraman, M., Srinivasan, H., et al. (2022). Single-cell and bulk transcriptome sequencing identifies two epithelial tumor cell states and refines the consensus molecular classification of colorectal cancer. Nat. Genet. *54*, 963–975. 10.1038/s41588-022-01100-4.

7. Nguyen, L.H., Goel, A., and Chung, D.C. (2020). Pathways of Colorectal Carcinogenesis. Gastroenterology *158*, 291–302. 10.1053/j.gastro.2019.08.059.

8. Bugter, J.M., Fenderico, N., and Maurice, M.M. (2021). Mutations and mechanisms of WNT pathway tumour suppressors in cancer. Nat. Rev. Cancer *21*, 5–21. 10.1038/s41568-020-00307-z.

9. Chen, B., Scurrah, C.R., McKinley, E.T., Simmons, A.J., Ramirez-Solano, M.A., Zhu, X., Markham, N.O., Heiser, C.N., Vega, P.N., Rolong, A., et al. (2021). Differential pre-malignant programs and microenvironment chart distinct paths to malignancy in human colorectal polyps. Cell *184*, 6262-6280.e26. 10.1016/j.cell.2021.11.031.

10. Yan, H.H.N.N., Lai, J.C.W.W., Ho, S.L., Leung, W.K., Law, W.L., Lee, J.F.Y.Y., Chan, A.S.Y.A.K.W.Y.A.K.W., Tsui, W.Y., Chan, A.S.Y.A.K.W.Y.A.K.W., Lee, B.C.H.H., et al. (2017). RNF43 germline and somatic mutation in serrated neoplasia pathway and its association with BRAF mutation. Gut *66*, 1645–1656. 10.1136/gutjnl-2016-311849.

11. McCarthy, A.J., Serra, S., and Chetty, R. (2019). Traditional serrated adenoma: an overview of pathology and emphasis on molecular pathogenesis. BMJ Open Gastroenterol. *6*, e000317. 10.1136/bmjgast-2019-000317.

12. Hashimoto, T., Ogawa, R., Yoshida, H., Taniguchi, H., Kojima, M., Saito, Y., and Sekine, S. (2019). Acquisition of WNT pathway gene alterations coincides with the transition from precursor polyps to traditional serrated adenomas. Am. J. Surg. Pathol. *43*, 132–139. 10.1097/PAS.0000000000001149.

13. Van De Wetering, M., Francies, H.E., Francis, J.M., Bounova, G., Iorio, F., Pronk, A., Van Houdt, W., Van Gorp, J., Taylor-Weiner, A., Kester, L., et al. (2015). Prospective derivation of a living organoid biobank of colorectal cancer patients. Cell *161*, 933–

945. 10.1016/j.cell.2015.03.053.

14. Elez, E., Ros, J., Fernández, J., Villacampa, G., Moreno-cárdenas, A.B., Arenillas, C., Bernatowicz, K., Comas, R., Li, S., Kodack, D.P., et al. (2022). RNF43 mutations predict response to anti-BRAF/EGFR combinatory therapies in BRAFV600E metastatic colorectal cancer. Nat. Med. *28*. 10.1038/s41591-022-01976-z.

15. Kleeman, S.O., Koelzer, V.H., Jones, H.J.S., Vazquez, E.G., Davis, H., East, J.E., Arnold, R., Koppens, M.A.J., Blake, A., Domingo, E., et al. (2020). Exploiting differential Wnt target gene expression to generate a molecular biomarker for colorectal cancer stratification. Gut *69*, 1092–1103. 10.1136/gutjnl-2019-319126.

16. Ubink, I., Bolhaqueiro, A.C.F., Elias, S.G., Raats, D.A.E., Constantinides, A., Peters, N.A., Wassenaar, E.C.E., de Hingh, I.H.J.T., Rovers, K.P., van Grevenstein, W.M.U., et al. (2019). Organoids from colorectal peritoneal metastases as a platform for improving hyperthermic intraperitoneal chemotherapy. Br. J. Surg. *106*, 1404–1414. 10.1002/bjs.11206.

17. Fumagalli, A., Suijkerbuijk, S.J.E., Begthel, H., Beerling, E., Oost, K.C., Snippert, H.J., Van Rheenen, J., and Drost, J. (2018). A surgical orthotopic organoid transplantation approach in mice to visualize and study colorectal cancer progression. Nat. Protoc. *13*, 235–247. 10.1038/nprot.2017.137.

18. Sasaki, N., Sachs, N., Wiebrands, K., Ellenbroek, S.I.J., Fumagalli, A., Lyubimova, A., Begthel, H., Van Born, M. Den, Van Es, J.H., Karthaus, W.R., et al. (2016). Reg4+ deep crypt secretory cells function as epithelial niche for Lgr5+ stem cells in colon. Proc. Natl. Acad. Sci. U. S. A. *113*, E5399–E5407. 10.1073/pnas.1607327113.

19. Wang, Y., Song, W., Wang, J., Wang, T., Xiong, X., Qi, Z., Fu, W., Yang, X., Chen, Y.G., and Chen, Y.G. (2020). Single-cell transcriptome analysis reveals differential

nutrient absorption functions in human intestine. J. Exp. Med. *217*. 10.1084/jem_20191130.

20. Krotenberg Garcia, A., van Rheenen, J., and Suijkerbuijk, S.J.E. (2021). Generation of mixed murine organoids to model cellular interactions. STAR Protoc. *2*, 100997. 10.1016/j.xpro.2021.100997.

21. Koo, B.K., Spit, M., Jordens, I., Low, T.Y., Stange, D.E., Van De Wetering, M., Van Es, J.H., Mohammed, S., Heck, A.J.R., Maurice, M.M., et al. (2012). Tumour suppressor RNF43 is a stem-cell E3 ligase that induces endocytosis of Wnt receptors. Nature *488*, 665–669. 10.1038/nature11308.

22. Sato, T., van Es, J.H., Snippert, H.J., Stange, D.E., Vries, R.G., van den Born, M., Barker, N., Shroyer, N.F., van de Wetering, M., and Clevers, H. (2011). Paneth cells constitute the niche for Lgr5 stem cells in intestinal crypts. Nature *469*, 415–418. 10.1038/nature09637.

23. Oost, K.C., van Voorthuijsen, L., Fumagalli, A., Lindeboom, R.G.H., Sprangers, J., Omerzu, M., Rodriguez-Colman, M.J., Heinz, M.C., Verlaan-Klink, I., Maurice, M.M., et al. (2018). Specific Labeling of Stem Cell Activity in Human Colorectal Organoids Using an ASCL2-Responsive Minigene. Cell Rep. *22*, 1600–1614. 10.1016/j.celrep.2018.01.033.

24. Rodríguez-Colman, M.J., Schewe, M., Meerlo, M., Stigter, E., Gerrits, J., Pras-Raves, M., Sacchetti, A., Hornsveld, M., Oost, K.C., Snippert, H.J., et al. (2017). Interplay between metabolic identities in the intestinal crypt supports stem cell function. Nature *543*, 424–427. 10.1038/nature21673.

25. Glover, L.E., Lee, J.S., and Colgan, S.P. (2016). Oxygen metabolism and barrier regulation in the intestinal mucosa. J. Clin. Invest. *126*, 3680–3688. 10.1172/JCI84429.

26. Huang, J., Pan, H., Wang, J., Wang, T., Huo, X., Ma, Y., Lu, Z., Sun, B., and Jiang, H. (2021). Unfolded protein response in colorectal cancer. Cell Biosci. *11*, 1–16. 10.1186/s13578-021-00538-z.

27. Sampson, L.L., Davis, A.K., Grogg, M.W., and Zheng, Y. (2016). MTOR disruption causes intestinal epithelial cell defects and intestinal atrophy postinjury in mice. FASEB J. *30*, 1263–1275. 10.1096/fj.15-278606.

28. He, G., Lin, L., DeMartino, J., Zheng, X., Staliarova, N., Dayton, T., Begthel, H., van de Wetering, W.J., Bodewes, E., van Zon, J., et al. (2022). Optimized human intestinal organoid model reveals interleukin-22-dependency of paneth cell formation. Cell Stem Cell, 1–13. 10.1016/j.stem.2022.08.002.

29. Cañellas-Socias, A., Cortina, C., Hernando-Momblona, X., Palomo-Ponce, S., Mulholland, E.J., Turon, G., Mateo, L., Conti, S., Roman, O., Sevillano, M., et al. (2022). Metastatic recurrence in colorectal cancer arises from residual EMP1+ cells. Nature. 10.1038/s41586-022-05402-9.

30. Vasquez, E.G., Nasreddin, N., Valbuena, G.N., Mulholland, E.J., Belnoue-Davis, H.L., Eggington, H.R., Schenck, R.O., Wouters, V.M., Wirapati, P., Gilroy, K., et al. (2022). Dynamic and adaptive cancer stem cell population admixture in colorectal neoplasia. Cell Stem Cell *29*, 1213-1228.e8. 10.1016/j.stem.2022.07.008.

31. Drost, J., Van Jaarsveld, R.H., Ponsioen, B., Zimberlin, C., Van Boxtel, R., Buijs, A., Sachs, N., Overmeer, R.M., Offerhaus, G.J., Begthel, H., et al. (2015). Sequential cancer mutations in cultured human intestinal stem cells. Nature *521*, 43–47. 10.1038/nature14415.

32. Giannakis, M., Hodis, E., Jasmine Mu, X., Yamauchi, M., Rosenbluh, J., Cibulskis, K., Saksena, G., Lawrence, M.S., Qian, Z.R., Nishihara, R., et al. (2014). RNF43 is

frequently mutated in colorectal and endometrial cancers. Nat. Genet. *46*, 1264–1266. 10.1038/ng.3127.

33. Michels, B.E., Mosa, M.H., Grebbin, B.M., Yepes, D., Darvishi, T., Hausmann, J., Urlaub, H., Zeuzem, S., Kvasnicka, H.M., Oellerich, T., et al. (2019). Human colon organoids reveal distinct physiologic and oncogenic Wnt responses. J. Exp. Med. *216*, 704–720. 10.1084/jem.20180823.

34. Uhlitz, F., Bischoff, P., Peidli, S., Sieber, A., Trinks, A., Lüthen, M., Obermayer, B., Blanc, E., Ruchiy, Y., Sell, T., et al. (2021). Mitogen-activated protein kinase activity drives cell trajectories in colorectal cancer. EMBO Mol. Med. *13*, 1–17. 10.15252/emmm.202114123.

35. Miller, S.A., Policastro, R.A., Sriramkumar, S., Lai, T., Huntington, T.D., Ladaika, C.A., Kim, D., Hao, C., Zentner, G.E., and O'Hagan, H.M. (2021). LSD1 and aberrant DNA methylation mediate persistence of enteroendocrine progenitors that support BRAF-mutant colorectal cancer. Cancer Res. *81*, 3791–3805. 10.1158/0008-5472.CAN-20-3562.

36. Shimokawa, M., Ohta, Y., Nishikori, S., Matano, M., Takano, A., Fujii, M., Date, S., Sugimoto, S., Kanai, T., and Sato, T. (2017). Visualization and targeting of LGR5+ human colon cancer stem cells. Nature *545*, 187–192. 10.1038/nature22081.

37. Morral, C., Stanisavljevic, J., Hernando-Momblona, X., Mereu, E., Álvarez-Varela, A., Cortina, C., Stork, D., Slebe, F., Turon, G., Whissell, G., et al. (2020). Zonation of Ribosomal DNA Transcription Defines a Stem Cell Hierarchy in Colorectal Cancer. Cell Stem Cell *26*, 845-861.e12. 10.1016/j.stem.2020.04.012.

38. Sacchetti, A., Teeuwssen, M., Verhagen, M., Joosten, R., Xu, T., Stabile, R., van der Steen, B., Watson, M.M., Gusinac, A., Kim, W.K., et al. (2021). Phenotypic plasticity

underlies local invasion and distant metastasis in colon cancer. Elife *10*, 1–28. 10.7554/eLife.61461.

39. Van Der Heijden, M., Miedema, D.M., Waclaw, B., Veenstra, V.L., Lecca, M.C., Nijman, L.E., Van Dijk, E., Van Neerven, S.M., Lodestijn, S.C., Lenos, K.J., et al. (2019). Spatiotemporal regulation of clonogenicity in colorectal cancer xenografts. Proc. Natl. Acad. Sci. U. S. A. *116*, 6140–6145. 10.1073/pnas.1813417116.

40. Fumagalli, A., Oost, K.C., Kester, L., Morgner, J., Bornes, L., Bruens, L., Spaargaren, L., Azkanaz, M., Schelfhorst, T., Beerling, E., et al. (2020). Plasticity of Lgr5-Negative Cancer Cells Drives Metastasis in Colorectal Cancer. Cell Stem Cell *26*, 569-578.e7. 10.1016/j.stem.2020.02.008.

41. Heinz, M.C., Peters, N.A., Oost, K.C., Lindeboom, R.G.H., van Voorthuijsen, L., Fumagalli, A., van der Net, M.C., de Medeiros, G., Hageman, J.H., Verlaan-Klink, I., et al. (2022). Liver Colonization by Colorectal Cancer Metastases Requires YAP-Controlled Plasticity at the Micrometastatic Stage. Cancer Res. *82*, 1953–1968. 10.1158/0008-5472.CAN-21-0933.

42. Fang, L., Ford-Roshon, D., Russo, M., O'Brien, C., Xiong, X., Gurjao, C., Grandclaudon, M., Raghavan, S., Corsello, S.M., Carr, S.A., et al. (2022). RNF43 G659fs is an oncogenic colorectal cancer mutation and sensitizes tumor cells to PI3K/mTOR inhibition. Nat. Commun. *13*, 1–12. 10.1038/s41467-022-30794-7.

43. Hoxhaj, G., and Manning, B.D. (2020). The PI3K–AKT network at the interface of oncogenic signalling and cancer metabolism. Nat. Rev. Cancer *20*, 74–88. 10.1038/s41568-019-0216-7.

44. Zhou, Y., Rychahou, P., Wang, Q., Weiss, H.L., and Evers, B.M. (2015). TSC2/mTORC1 signaling controls Paneth and goblet cell differentiation in the

intestinal epithelium. Cell Death Dis. *6*, 1–10. 10.1038/cddis.2014.588.

45. Araujo, A., Safronova, A., Burger, E., López-Yglesias, A., Giri, S., Camanzo, E.T., Martin, A.T., Grivennikov, S., and Yarovinsky, F. (2021). IFN-γ mediates Paneth cell death via suppression of mTOR. Elife *10*, 1–19. 10.7554/eLife.60478.

46. Hugen, N., Brown, G., Glynne-Jones, R., De Wilt, J.H.W., and Nagtegaal, I.D. (2016). Advances in the care of patients with mucinous colorectal cancer. Nat. Rev. Clin. Oncol. *13*, 361–369. 10.1038/nrclinonc.2015.140.

47. Kufe, D.W. (2009). Mucins in cancer: function, prognosis and therapy. Nat. Rev. Cancer *9*, 874–885. 10.1038/nrc2761.

48. Ryland, G.L., Hunter, S.M., Doyle, M.A., Rowley, S.M., Christie, M., Allan, P.E., Bowtell, D.D., Gorringe, K.L., and Campbell, I.G. (2013). RNF43 is a tumour suppressor gene mutated in mucinous tumours of the ovary. J. Pathol. *229*, 469–476. 10.1002/path.4134.

49. Lee, J.H., Kim, Y., Choi, J.W., and Kim, Y.S. (2016). KRAS, GNAS, and RNF43 mutations in intraductal papillary mucinous neoplasm of the pancreas: a meta-analysis. Springerplus *5*. 10.1186/s40064-016-2847-4.

50. Sakamoto, H., Kuboki, Y., Hatori, T., Yamamoto, M., Sugiyama, M., Shibata, N., Shimizu, K., Shiratori, K., and Furukawa, T. (2015). Clinicopathological significance of somatic RNF43 mutation and aberrant expression of ring finger protein 43 in intraductal papillary mucinous neoplasms of the pancreas. Mod. Pathol. *28*, 261–267. 10.1038/modpathol.2014.98.

51. Sheffer, M., Bacolod, M.D., Zuk, O., Giardina, S.F., Pincas, H., Barany, F., Paty, P.B., Gerald, W.L., Notterman, D.A., and Domany, E. (2009). Association of survival and

disease progression with chromosomal instability: A genomic exploration of colorectal cancer. Proc. Natl. Acad. Sci. U. S. A. *106*, 7131–7136. 10.1073/pnas.0902232106.

52. Van der Flier, L.G., Sabates-Bellver, J., Oving, I., Haegebarth, A., De Palo, M., Anti, M., Van Gijn, M.E., Suijkerbuijk, S., Van de Wetering, M., Marra, G., et al. (2007). The Intestinal Wnt/TCF Signature. Gastroenterology *132*, 628–632. 10.1053/j.gastro.2006.08.039.

53. Miao, Y., Ha, A., de Lau, W., Yuki, K., Santos, A.J.M., You, C., Geurts, M.H., Puschhof, J., Pleguezuelos-Manzano, C., Peng, W.C., et al. (2020). Next-Generation Surrogate Wnts Support Organoid Growth and Deconvolute Frizzled Pleiotropy In Vivo. Cell Stem Cell *27*, 840-851.e6. 10.1016/j.stem.2020.07.020.

54. Bollen, Y., Post, J., Koo, B.-K., and Snippert, H.J.G. (2018). How to create state-of-the-art genetic model systems: strategies for optimal CRISPR-mediated genome editing. Nucleic Acids Res. *46*, 6435–6454. 10.1093/nar/gky571.

55. Richardson, C.D., Ray, G.J., DeWitt, M.A., Curie, G.L., and Corn, J.E. (2016). Enhancing homology-directed genome editing by catalytically active and inactive CRISPR-Cas9 using asymmetric donor DNA. Nat. Biotechnol. *34*, 339–344. 10.1038/nbt.3481.

56. Bollen, Y., Hageman, J.H., van Leenen, P., Derks, L.L.M., Ponsioen, B., Buissant des Amorie, J.R., Verlaan-Klink, I., van den Bos, M., Terstappen, L.W.M.M., van Boxtel, R., et al. (2022). Efficient and error-free fluorescent gene tagging in human organoids without double-strand DNA cleavage. PLoS Biol. *20*, 1–16. 10.1371/journal.pbio.3001527.

57. Fujii, M., Matano, M., Nanki, K., and Sato, T. (2015). Efficient genetic engineering of human intestinal organoids using electroporation. Nat. Protoc. *10*, 1474–1485.

10.1038/nprot.2015.088.

58. Brinkman, E.K., Chen, T., Amendola, M., and Van Steensel, B. (2014). Easy quantitative assessment of genome editing by sequence trace decomposition. Nucleic Acids Res. *42*, 1–8. 10.1093/nar/gku936.

59. Brinkman, E.K., Kousholt, A.N., Harmsen, T., Leemans, C., Chen, T., Jonkers, J., and van Steensel, B. (2018). Easy quantification of template-directed CRISPR/Cas9 editing. Nucleic Acids Res. *46*, e58. 10.1093/nar/gky164.

60. Li, H., and Durbin, R. (2010). Fast and accurate long-read alignment with Burrows-Wheeler transform. Bioinformatics *26*, 589–595. 10.1093/bioinformatics/btp698.

61. Tarasov, A., Vilella, A.J., Cuppen, E., Nijman, I.J., and Prins, P. (2015). Sambamba: Fast processing of NGS alignment formats. Bioinformatics *31*, 2032–2034. 10.1093/bioinformatics/btv098.

62. McKenna, A., Hanna, M., Banks, E., Sivachenko, A., Cibulskis, K., Kernytsky, A., Garimella, K., Altshuler, D., Gabriel, S., Daly, M., et al. (2010). The Genome Analysis Toolkit: A MapReduce framework for analyzing next-generation DNA sequencing data. Genome Res. *20*, 1297–1303. 10.1101/gr.107524.110.

63. Boeva, V., Popova, T., Bleakley, K., Chiche, P., Cappo, J., Schleiermacher, G., Janoueix-Lerosey, I., Delattre, O., and Barillot, E. (2012). Control-FREEC: A tool for assessing copy number and allelic content using next-generation sequencing data. Bioinformatics *28*, 423–425. 10.1093/bioinformatics/btr670.

64. Cingolani, P., Patel, V.M., Coon, M., Nguyen, T., Land, S.J., Ruden, D.M., and Lu, X. (2012). Using Drosophila melanogaster as a model for genotoxic chemical mutational studies with a new program, SnpSift. Front. Genet. *3*, 1–9. 10.3389/fgene.2012.00035.

65. Cingolani, P., Platts, A., Wang, L.L., Coon, M., Nguyen, T., Wang, L., Land, S.J., Lu, X., and Ruden, D.M. (2012). A program for annotating and predicting the effects of single nucleotide polymorphisms, SnpEff: SNPs in the genome of Drosophila melanogaster strain w1118; iso-2; iso-3. Fly (Austin). *6*, 80–92. 10.4161/fly.19695.

66. Gu, Z., Eils, R., and Schlesner, M. (2016). Complex heatmaps reveal patterns and correlations in multidimensional genomic data. Bioinformatics *32*, 2847–2849. 10.1093/bioinformatics/btw313.

67. Shale, C., Cameron, D.L., Baber, J., Wong, M., Cowley, M.J., Papenfuss, A.T., Cuppen, E., and Priestley, P. (2022). Unscrambling cancer genomes via integrated analysis of structural variation and copy number. Cell Genomics *2*, 100112. 10.1016/j.xgen.2022.100112.

68. Bankhead, P., Loughrey, M.B., Fernández, J.A., Dombrowski, Y., McArt, D.G., Dunne, P.D., McQuaid, S., Gray, R.T., Murray, L.J., Coleman, H.G., et al. (2017). QuPath: Open source software for digital pathology image analysis. Sci. Rep. *7*, 1–7. 10.1038/s41598-017-17204-5.

69. Dobin, A., Davis, C.A., Schlesinger, F., Drenkow, J., Zaleski, C., Jha, S., Batut, P., Chaisson, M., and Gingeras, T.R. (2013). STAR: Ultrafast universal RNA-seq aligner. Bioinformatics *29*, 15–21. 10.1093/bioinformatics/bts635.

70. Love, M.I., Huber, W., and Anders, S. (2014). Moderated estimation of fold change and dispersion for RNA-seq data with DESeq2. Genome Biol. *15*, 1–21. 10.1186/s13059-014-0550-8.

71. Liberzon, A., Birger, C., Thorvaldsdóttir, H., Ghandi, M., Mesirov, J.P., and Tamayo, P. (2015). The Molecular Signatures Database Hallmark Gene Set Collection. Cell Syst. *1*, 417–425. 10.1016/j.cels.2015.12.004.

72. Uhlén, M., Fagerberg, L., Hallström, B.M., Lindskog, C., Oksvold, P., Mardinoglu, A., Sivertsson, Å., Kampf, C., Sjöstedt, E., Asplund, A., et al. (2015). Tissue-based map of the human proteome. Science (80-.). *347*. 10.1126/science.1260419.

73. Muraro, M.J., Dharmadhikari, G., Grün, D., Groen, N., Dielen, T., Jansen, E., van Gurp, L., Engelse, M.A., Carlotti, F., de Koning, E.J.P., et al. (2016). A Single-Cell Transcriptome Atlas of the Human Pancreas. Cell Syst. *3*, 385-394.e3. 10.1016/j.cels.2016.09.002.

74. Hao, Y., Hao, S., Andersen-Nissen, E., Mauck, W.M., Zheng, S., Butler, A., Lee, M.J., Wilk, A.J., Darby, C., Zager, M., et al. (2021). Integrated analysis of multimodal single-cell data. Cell *184*, 3573-3587.e29. 10.1016/j.cell.2021.04.048.

75. Chen, E.Y., Tan, C.M., Kou, Y., Duan, Q., Wang, Z., Meirelles, G.V., Clark, N.R., and Ma'ayan, A. (2013). Enrichr: interactive and collaborative HTML5 gene list enrichment analysis tool. BMC Bioinformatics *14*, 128. 10.1186/1471-2105-14-128.

76. Korsunsky, I., Millard, N., Fan, J., Slowikowski, K., Zhang, F., Wei, K., Baglaenko, Y., Brenner, M., Loh, P. ru, and Raychaudhuri, S. (2019). Fast, sensitive and accurate integration of single-cell data with Harmony. Nat. Methods *16*, 1289–1296. 10.1038/s41592-019-0619-0.

77. Guinney, J., Dienstmann, R., Wang, X., de Reyniès, A., Schlicker, A., Soneson, C., Marisa, L., Roepman, P., Nyamundanda, G., Angelino, P., et al. (2015). The consensus molecular subtypes of colorectal cancer. Nat. Med. *21*, 1350–1356. 10.1038/nm.3967.

78. Schmidt, U., Weigert, M., Broaddus, C., and Myers, G. (2018). Cell Detection with Star-Convex Polygons. In, A. F. Frangi, J. A. Schnabel, C. Davatzikos, C. Alberola-López, and G. Fichtinger, eds. (Springer International Publishing), pp. 265–273. 10.1007/978-3-030-00934-2_30.

79. Bolhaqueiro, A.C.F., van Jaarsveld, R.H., Ponsioen, B., Overmeer, R.M., Snippert, H.J., and Kops, G.J.P.L. (2018). Live imaging of cell division in 3D stem-cell organoid cultures. Methods Cell Biol. *145*, 91–106. 10.1016/bs.mcb.2018.03.016.

80. Kim, S.K., Kim, S.Y., Kim, J.H., Roh, S.A., Cho, D.H., Kim, Y.S., and Kim, J.C. (2014). A nineteen gene-based risk score classifier predicts prognosis of colorectal cancer patients. Mol. Oncol. *8*, 1653–1666. 10.1016/j.molonc.2014.06.016.